J. Fluid Mech. (1990), *vol.* 220, *pp.* 427–458
Printed in Great Britain

Material-element deformation in isotropic turbulence

By S. S. GIRIMAJI AND S. B. POPE
Sibley School of Mechanical and Aerospace Engineering, Cornell University, Ithaca, NY 14853, USA

(Received 9 October 1989 and in revised form 27 April 1990)

The evolution of infinitesimal material line and surface elements in homogeneous isotropic turbulence is studied using velocity-gradient data generated by direct numerical simulations (DNS). The mean growth rates of length ratio (l) and area ratio (A) of material elements are much smaller than previously estimated by Batchelor (1952) owing to the effects of vorticity and of non-persistent straining. The probability density functions (p.d.f.'s) of $l/\langle l\rangle$ and $A/\langle A\rangle$ do not attain stationarity as hypothesized by Batchelor (1952). It is shown analytically that the random variable $l/\langle l\rangle$ cannot be stationary if the variance and integral timescale of the strain rate along a material line are non-zero and DNS data confirm that this is indeed the case. The application of the central limit theorem to the material element evolution equations suggests that the standardized variables $\hat{l}(\equiv(\ln l-\langle\ln l\rangle)/(\mathrm{var}\, l)^{\frac{1}{2}})$ and $\hat{A}(\equiv(\ln A-\langle\ln A\rangle)/(\mathrm{var}\, A)^{\frac{1}{2}})$ should attain stationary distributions that are Gaussian for all Reynolds numbers. The p.d.f.s of $\hat{l}$ and $\hat{A}$ calculated from DNS data appear to attain stationary shapes that are independent of Reynolds number. The stationary values of the flatness factor and super-skewness of both $\hat{l}$ and $\hat{A}$ are in close agreement with those of a Gaussian distribution. Moreover, the mean and variance of $\ln l$ (and $\ln A$) grow linearly in time (normalized by the Kolmogorov timescale, τ_η), at rates that are nearly independent of Reynolds number. The statistics of material volume-element deformation are also studied and are found to be nearly independent of Reynolds number. An initially spherical infinitesimal volume of fluid deforms into an ellipsoid. It is found that the largest and the smallest of the principal axes grow and shrink respectively, exponentially in time at comparable rates. Consequently, to conserve volume, the intermediate principal axis remains approximately constant.

The performance of the stochastic model of Girimaji & Pope (1990) for the velocity gradients is also studied. The model estimates of the growth rates of $\langle\ln l\rangle$ and $\langle\ln A\rangle$ are close to the DNS values. The growth rate of the variances are estimated by the model to within 17%. The stationary distributions of $\hat{l}$ and $\hat{A}$ obtained from the model agree very well with those calculated from DNS data. The model also performs well in calculating the statistics of material volume-element deformation.

1. Introduction

The evolution of material lines, surfaces and volumes in turbulence is of intrinsic interest and practical value. Vortex lines in the inviscid limit, and the magnetic lines of force in media of high conductivity are examples of vector fields that are proportional to material-line-element vectors (Monin & Yaglom 1975). Constant-property surfaces of temperature or of other passive scalars are material surfaces in the limit of negligible molecular diffusivity (Pope 1988). In premixed combustion, for laminar flame speeds small compared with the Kolmogorov velocity scale, the

flamelets are trapped close to material surfaces that they were initially coincident with (Yeung, Girimaji & Pope 1989). So a good understanding of the evolution of surfaces in turbulence is important for accurate modelling of the scalar-mixing and the flamelet propagation aspects of combustion.

A material element is defined as any line, surface or volume that always consists of the same material points or fluid particles. The basic diffusive character of turbulence – which tends to move two fluid particles, however close initially, away from each other – renders the study of finite-sized lines and surfaces difficult. Batchelor (1952) was the first to simplify the general analysis of lines and surfaces to the analysis of infinitesimal line and surface elements. As Batchelor observed, subject to the assumption that velocity gradients in turbulence are bounded, an initially infinitesimal material element remains infinitesimal for a finitely long time, and during this period the velocity gradients can be considered uniform over the material element. So a one-point description of the velocity gradients following fluid particles suffices for the study of the evolution of infinitesimal elements.

An infinitesimal line element $\boldsymbol{e}$ evolves according to

$$\frac{\mathrm{d}e_i}{\mathrm{d}T} = U_{ij}\, e_j, \tag{1}$$

where T is time, and $\boldsymbol{U}$ is the velocity-gradient tensor following the fluid particle associated with the fluid element. Batchelor further argues that after an initial transient period, the statistics of the line element evolution will be independent of its initial orientation, although the length itself will still be small enough for the element to experience uniform strain. The period of validity of this assumption will be referred to from here on as the *steady state*.

Consider a material line of finite length ($E(T)$ at time T) to be composed of a large number ($N_\infty, N_\infty \to \infty$) of infinitesimal line element vectors $\boldsymbol{e}_n (n = 1, 2, \ldots, N_\infty)$, such that,

$$E(T) = \sum_{n=1}^{N_\infty} |\boldsymbol{e}_n(T)|. \tag{2}$$

If, at time $T = 0$, the lengths of all the infinitesimal elements are the same then

$$\frac{E(T)}{E(0)} = \frac{|\boldsymbol{e}(0)|}{E(0)} \sum_{n=1}^{N_\infty} \frac{|\boldsymbol{e}_n(T)|}{|\boldsymbol{e}(0)|}, \tag{3}$$

where

$$E(0) = N_\infty\, |\boldsymbol{e}(0)|, \tag{4}$$

so that

$$\frac{E(T)}{E(0)} = \frac{1}{N_\infty} \sum_{n=1}^{N_\infty} \frac{|\boldsymbol{e}_n(T)|}{|\boldsymbol{e}(0)|}. \tag{5}$$

But in homogeneous turbulence the evolution of each of the infinitesimal material elements is statistically identical at steady state and hence

$$\left\langle \frac{E(T)}{E(0)} \right\rangle = \left\langle \frac{|\boldsymbol{e}(T)|}{|\boldsymbol{e}(0)|} \right\rangle, \tag{6}$$

where the angular brackets indicate the ensemble average over independently evolving infinitesimal material-line elements. The evaluation of the higher moments of $E(T)$ in terms of the infinitesimal elements involve the joint statistics of neighbouring elements which are difficult to compute, as discussed before, owing to the diffusive nature of turbulence.

In this work we study an ensemble of incontiguous, perhaps independently evolving, infinitesimal line elements ($\boldsymbol{e}$) and area elements ($\boldsymbol{f}$) at steady state. As seen above the average length (or area) of infinitesimal elements can be calculated directly from the mean of $\boldsymbol{e}$ (or $\boldsymbol{f}$). Although the higher moments cannot be calculated using this approach the study of incontiguous elements should provide valuable insight into the evolution of finite lines and surfaces.

1.1. *Definitions*

For simplicity we define

$$e(t) \equiv |\boldsymbol{e}(t)|,$$
$$f(t) \equiv |\boldsymbol{f}(t)|.$$

We further define the length ratio ($\boldsymbol{l}$) and area ratio ($\boldsymbol{A}$) as

$$\boldsymbol{l}(t) \equiv \frac{\boldsymbol{e}(t)}{e(0)}, \tag{7}$$

$$\boldsymbol{A}(t) \equiv \frac{\boldsymbol{f}(t)}{f(0)}. \tag{8}$$

Also we define $l(t)$ and $A(t)$ as the magnitudes of $\boldsymbol{l}(t)$ and $\boldsymbol{A}(t)$, respectively, which (by their definitions) are initially unity. The linearity of the evolution equation (1) permits direct calculation of $l(t)$, from which $e(t)$ can be computed if $e(0)$ is known.

The material volume element deformation quantities of interest are the angles θ and α, and the Cauchy–Green tensor ($\boldsymbol{W}$) of deformation. The angles θ and α are defined as follows: θ is the angle between two material line elements that are initially orthogonal; and α is the angle between the normal to a material plane and a material line that is initially its normal. The angle θ indicates the extent to which two initially perpendicular lines become colinear, whereas α indicates the extent to which two initially parallel planes get closer. Further, Γ_l is defined as the angle between a material line vector $\boldsymbol{e}$ and the instantaneous maximum positive strain-rate direction $\boldsymbol{P}$ associated with that material element. Finally Γ_A is defined as the angle between an area normal $\boldsymbol{f}$ and the instantaneous maximum negative strain-rate direction, $\boldsymbol{C}$.

Throughout the rest of the paper we deal with non-dimensional quantities. The velocity gradients and time are normalized by the Kolmogorov timescale τ_η, so that

$$t = T/\tau_\eta,$$
$$\boldsymbol{h} = \boldsymbol{U}\tau_\eta.$$

Further, let s_{ij} be the symmetric (strain-rate tensor) part, and r_{ij} be the antisymmetric (rotation-rate tensor) part, of the velocity-gradient tensor h_{ij} following a fluid particle. Let a_1, a_2 and a_3 be the principal values of s_{ij} ordered such that,

$$a_1 \geqslant a_2 \geqslant a_3.$$

As a consequence of the incompressibility condition, that $s_{ii} = 0$, we have

$$a_1 \geqslant 0, \quad a_3 \leqslant 0.$$

It is known from previous works (Ashurst *et al.* 1987) that $\langle a_2 \rangle$ is positive.

Equation (1) implies the following growth-rate equations for $\ln(e_i e_i)$ and $\ln(f_i f_i)$:

$$\zeta \equiv \frac{\mathrm{d}\ln e}{\mathrm{d}t} = \frac{\mathrm{d}\ln l}{\mathrm{d}t} = s_{ij} e'_i e'_j, \tag{9}$$

$$\xi \equiv \frac{\mathrm{d}\ln f}{\mathrm{d}t} = \frac{\mathrm{d}\ln A}{\mathrm{d}t} = -s_{ij} N_i N_j. \tag{10}$$

In the above equations $\boldsymbol{e}'$ is the unit vector in the $\boldsymbol{e}$-direction and $\boldsymbol{N}(\equiv \boldsymbol{f}/f)$ is the area normal. The growth rates ζ and ξ are composed of the strain-rate tensor and a vector of unit magnitude. Hence at steady state when the strain-rate tensor is stationary, Batchelor (1952) argues that the statistics of ζ and ξ can only be either stationary or cyclic with time-independent finite amplitude. Since the latter possibility is unphysical the random variables ζ and ξ must be stationary at steady state. As can be seen from (9) and (10), the angles Γ_l and Γ_A play an important role in determining ζ and ξ.

1.2. *A brief literature survey*

Since Batchelor (1952), there have been others who have analysed the growth of infinitesimal material-line elements. Cocke (1969) and Orszag (1970) prove to varying degrees of rigour that the length of a line element increases on average in a turbulent velocity field. Batchelor (1952) and Batchelor & Townsend (1956) have studied the evolution under the assumption of persistent straining – an assumption that they claim is supported by the experiment of Townsend (1951). Monin & Yaglom (1975, §24.5) study the evolution in the case when the effect of vorticity is exactly offset by the rotation of the strain-rate axes. The important conclusions reached in Batchelor (1952) and Monin & Yaglom (1975) are:

(i) Material line elements tend to orient themselves along the principal axis corresponding to the maximum positive strain rate (a_1). So at steady state, with perfect alignment (i.e. $\Gamma_l = 0$), (9) yields

$$\langle \zeta \rangle = \langle a_1 \rangle.$$

(ii) Material area elements lie in the plane of the a_1 and a_2 principal strain-rate axes (i.e. $\Gamma_A = 0$). So at steady state, from (10)

$$\langle \xi \rangle = \langle a_1 + a_2 \rangle.$$

(iii) The probability density function (p.d.f.) of the scaled parameter $(l/\langle l \rangle)$ at steady state is self-similar (Batchelor 1952).

Kraichnan (1974) analyses the evolution of material elements in the other extreme case of a rapidly changing velocity (white-noise) field. Two of the relevant conclusions of this work are: (i) In reflection-invariant turbulence, the statistics of the growth rates of the logarithm of the length and area of infinitesimal material elements are identical. (ii) The length and area of material elements are log-normally distributed.

Recently the evolution of material elements has been studied using a simple stochastic velocity field by Drummond & Münch (1990*a*, *b*). They suggest that each moment of l (and similarly A) is associated with a timescale, and all these timescales need to be accounted for in determining the self-similar steady-state probability distribution of l. They go on to determine the relationship between these various moments. Concurrent with the present study the evolution of the curvature of material elements has been studied using a direct numerical simulation (DNS)-generated velocity field by Pope, Yeung & Girimaji (1989).

1.3. *Scope of the present work*

The objectives of this paper are to understand the physics of the evolution of infinitesimal material lines, surfaces and volumes in homogeneous isotropic turbulence, and to assess the performance of the stochastic velocity-gradient model of Girimaji & Pope (1990). In particular we address the following questions.

(i) Are the mean growth rates of line and area elements as previously estimated?

(ii) Is the p.d.f. of the scaled parameter $(l/\langle l \rangle)$ self-similar at steady state as suggested by Batchelor? If not, does any other scaling of length and area lead to self-similar p.d.f.s?

(iii) How do material volume elements deform in turbulence? To what shape does an initially spherical volume of fluid deform?

(iv) How does the stochastic model of Girimaji & Pope (1990) perform in calculating various details of material element deformation?

The organization of the rest of the paper is as follows. In §2 we discuss briefly how the Lagrangian data from DNS and the stochastic velocity-gradient model are used to calculate material element properties. The first, second, third and fourth questions listed above are then addressed in §§3, 4, 5 and 6 respectively. Section 7 summarizes our conclusions.

2. Determination of material element properties

In this paper all infinitesimal material element statistics are calculated from velocity-gradient time series (following fluid particles) using (1). The velocity-gradient time series are obtained in two ways: from direct numerical simulations, and from the stochastic model for velocity gradients of Girimaji & Pope (1990).

2.1. *Velocity-gradient time series from DNS*

The DNS Lagrangian velocity-gradient data are obtained from the stationary, isotropic turbulence calculations performed by Yeung & Pope (1989). They solve the instantaneous Navier–Stokes equations with periodic boundary conditions using a modified version of Rogallo's pseudo-spectral code (Rogallo 1981). The equations for Eulerian velocity are marched in time in spectral space from a random initial field. The nonlinear terms, however, are computed in physical space to avoid the expensive convolution-integral computations. The statistical stationarity of the turbulent velocity field is achieved in the simulations by adding energy isotropically to the low-wavenumbers in a way that leaves the high-wavenumber statistics relatively unaffected (Eswaran & Pope 1988). Using 128^3 uniformly spaced grid points, Taylor-scale Reynolds numbers R_λ of 38, 64 and 90 are achieved for different values of kinematic viscosity.

The spatial resolution is characterized by $k_{\max}\eta$, where $k_{\max}$ is the magnitude of the highest resolved wavenumber and η is the Kolmogorov lengthscale. For the case with the worst spatial resolution ($R_\lambda = 90$), $k_{\max}\eta$ is approximately 1.5, corresponding to a grid spacing of about twice the Kolmogorov lengthscale. Previous numerical studies have shown that this represents excellent resolution (Eswaran & Pope 1988; Yeung & Pope 1988). A constant time-step corresponding to a Courant number of about $\frac{1}{2}$ is used. For the case of worst temporal resolution ($R_\lambda = 90$), this time-step corresponds to approximately $\frac{1}{35}$ of the Kolmogorov timescale, τ_η.

The DNS Lagrangian velocity-gradient time series is obtained by tracking 4096 initially randomly placed particles over a period of approximately 30 Kolmogorov timescales. The velocity gradients of fluid particles (that fall between grid nodes) are obtained by interpolation, using highly accurate cubic splines (Yeung & Pope 1988). Numerical parameters and some important Eulerian statistics of the three simulations are presented in table 1.

Taylor-scale Reynolds number	R_λ	38	63	90
Grid size	N	128	128	128
Length of solution domain	L_0	2π	2π	2π
Kinematic viscosity	ν	0.025	0.0105	0.006546
Turbulence intensity	u'	1.582	1.637	1.274
Dissipation rate	$\langle\epsilon\rangle$	2.651	2.673	0.780
Longitudinal integral lengthscale L_1	$L_1/(\frac{1}{2}L_0)$	0.383	0.321	0.448
Dissipation timescale $\tau_\epsilon = \frac{3}{2}u'^2/\langle\epsilon\rangle$	τ_ϵ	1.420	1.510	3.174
Eddy turnover time $T_e = L_1/u'$	T_e/τ_ϵ	0.534	0.407	0.343
Kolmogorov timescale τ_η	τ_η/τ_ϵ	0.068	0.041	0.029
Duration of simulation T	T/T_e	5.32	5.85	5.51
Time-step Δt	$\Delta t/\tau_\eta$	0.012	0.024	0.027
Kolmogorov lengthscale η	η/L_1	0.041	0.025	0.018
Maximum resolved wavenumber k_{max}	$k_{max}\eta$	2.96	1.54	1.48
Taylor microscale λ	λ/L_1	0.500	0.399	0.326

TABLE 1. Numerical parameters and Eulerian statistics

2.2. *Velocity-gradient time series from the model*

The stochastic model of Girimaji & Pope (1990) models the velocity gradient following a fluid particle, h_{ij}, as a diffusion process. With the variance (σ^2), the integral timescale (τ_1) of $\ln(h_{ij}h_{ij})$ and the Kolmogorov timescale (τ_η) as the only input parameters, the model generates velocity-gradient (h_{ij}) time series. Time series for various Reynolds numbers are obtained by inputting into the model the corresponding DNS values of σ^2, τ_1 and τ_η. The model is used to generate velocity-gradient time series of 4000 particles over a period of approximately $25\tau_\eta$. Further details of the model and the numerical methods used to generate the time series are available in Girimaji & Pope (1990).

2.3. *Extraction of material-element data*

Once the velocity-gradient time series are available, the material-element deformation quantities of interest are calculated as follows. As mentioned in the previous Section, the linearity of the material deformation equation (1), permits us to deal with the length ratio (l) and area ratio (A) rather than their infinitesimal counterparts e and f. Referring to Monin & Yaglom (1975), a material-line element which is initially $\boldsymbol{l}(0)$, is given at any later time t by

$$\boldsymbol{l}(t) = \boldsymbol{B}(t)\cdot\boldsymbol{l}(0), \tag{11}$$

where $\boldsymbol{B}$ evolves by the equation

$$\frac{\mathrm{d}}{\mathrm{d}t}\boldsymbol{B} = \boldsymbol{h}(t)\cdot\boldsymbol{B}(t), \tag{12}$$

with the initial condition $\boldsymbol{B}(0) = \boldsymbol{I}$. The tensor $\boldsymbol{B}(t)$ contains all of the one-point infinitesimal material-element information at time t. Equation (12) is solved numerically for $\boldsymbol{B}$ using an accurate fourth-order Runge–Kutta scheme explained in the Appendix. Once $\boldsymbol{B}(t)$ is known, $\boldsymbol{l}(t)$ can be easily calculated from (11).

For each infinitesimal material element we consider a triplet of lines ($\boldsymbol{l}^1(t)$, $\boldsymbol{l}^2(t)$, $\boldsymbol{l}^3(t)$) that are initially orthogonal and oriented randomly with their respective strain-rate axes:

$$|\boldsymbol{l}^\alpha(0)| = 1, \quad \boldsymbol{l}^\alpha(0)\cdot\boldsymbol{l}^\beta(0) = \delta_{\alpha\beta} \quad \text{for} \quad \alpha, \beta = 1, 2, 3. \tag{13}$$

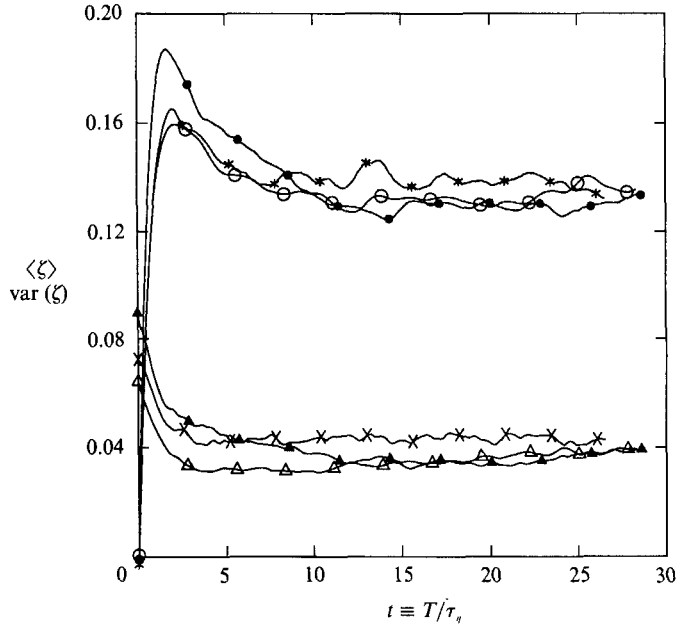

FIGURE 1. Mean and variance of the growth rate of $\ln l$, ζ: ○, ●, *, $\langle\zeta\rangle$ for $R_\lambda = 38, 63, 90$; △, ▲, ×, var(ζ) for $R_\lambda = 38, 63, 90$.

	$Re_\lambda = 38$	$Re_\lambda = 63$	$Re_\lambda = 93$
$\langle\zeta\rangle$	0.138	0.129	0.140
$\langle\xi\rangle$	0.163	0.159	0.173
var(ζ)	0.0441	0.0361	0.0436
var(ξ)	0.0913	0.0944	0.1134
T_ζ var(ζ)	0.0491	0.0488	0.0528
T_ξ var(ξ)	0.0892	0.0945	0.104

TABLE 2. Statistics of ζ and ξ

Knowledge of all three line element vectors at any time t enables us to calculate the statistics not only of $l(t)$ but also of the other material-element deformation quantities of interest (see §1.2), using the following simple trigonometric relations:

$$\boldsymbol{A}(t) = \boldsymbol{l}^1 \times \boldsymbol{l}^2, \tag{14}$$

$$\sin|\theta| = |\boldsymbol{A}|/(|\boldsymbol{l}^1||\boldsymbol{l}^2|), \tag{15}$$

$$\cos|\alpha| = |\boldsymbol{A}\cdot\boldsymbol{l}^3|/(|\boldsymbol{A}||\boldsymbol{l}^3|), \tag{16}$$

$$\cos\Gamma_l = |\boldsymbol{l}^1\cdot\boldsymbol{P}|/|\boldsymbol{l}^1|, \tag{17}$$

$$\cos\Gamma_A = |\boldsymbol{A}\cdot\boldsymbol{C}|/|\boldsymbol{A}|, \tag{18}$$

$$\boldsymbol{W} = \boldsymbol{B}\cdot\boldsymbol{B}^{\mathrm{T}}. \tag{19}$$

The signs of the directions of the vectors $\boldsymbol{l}^1$, $\boldsymbol{l}^2$, $\boldsymbol{l}^3$, $\boldsymbol{A}$, $\boldsymbol{P}$ and $\boldsymbol{C}$ are arbitrary and we are only interested in the magnitudes of the angles θ, α, Γ_l and Γ_A.

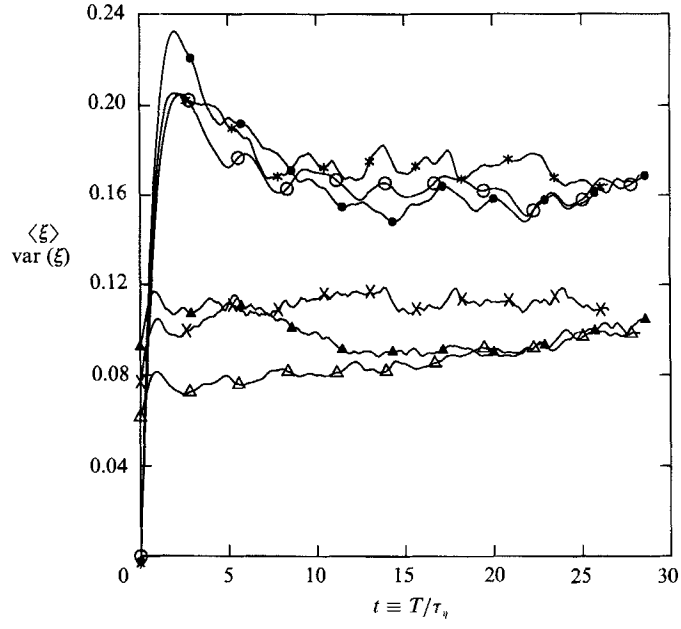

FIGURE 2. Mean and variance of the growth rate of $\ln A$, ξ: legend as figure 1.

3. Analysis of the mean growth rates of $\ln l$ and $\ln A$

In figure 1 the temporal evolution of the mean and variance of the line growth rate, ζ (equation (9)), is presented for various Reynolds numbers for $t = 0$–30. Figure 2 presents similar plots of the area growth rate, ξ (equation (10)). The steady-state ($t > 12$) values of the means and variances (obtained from time-averaging over $12\tau_\eta$–$25\tau_\eta$) of ζ and ξ are provided in table 2. On the figures and the table we make the following observations: (i) The transient evolution of $\ln l$ and $\ln A$ show some variation with Reynolds number, but the statistical error involved in the calculations are of the same order as the difference and hence no trends can be inferred. (ii) The steady-state growth rates (normalized by τ_η) vary somewhat with Reynolds number, but again no systematic trend can be adduced. (The slight difference in the values of $\langle\xi\rangle$ and var(ξ) between table 2 and those presented in Yeung *et al.* (1990) is due to the fact that slightly different values of Kolmogorov timescale τ_η have been used to calculate these quantities. The τ_η-values used in the present case are given in table 1.) (iii) The mean growth rates exhibit a peak at about $t = 2$ before settling to lower steady-state values. (iv) The steady-state values $\langle\zeta\rangle \approx 0.13$ and $\langle\xi\rangle \approx 0.16$ are much lower than their respective estimates $\langle a_1\rangle$ and $\langle a_1 + a_2\rangle$ (see §1.2), which from DNS data are 0.40 and 0.50. The values of $\langle a_1\rangle$ and $\langle a_1 + a_2\rangle$ computed from DNS data given above agree well with the theoretical estimates given in Monin & Yaglom (1975).

The first two observations are as anticipated since the evolution of infinitesimal elements is a small-scale phenomenon which when suitably scaled can be expected to be independent of Reynolds number. The last two observations are, however, surprising and are studied in detail in the rest of this section.

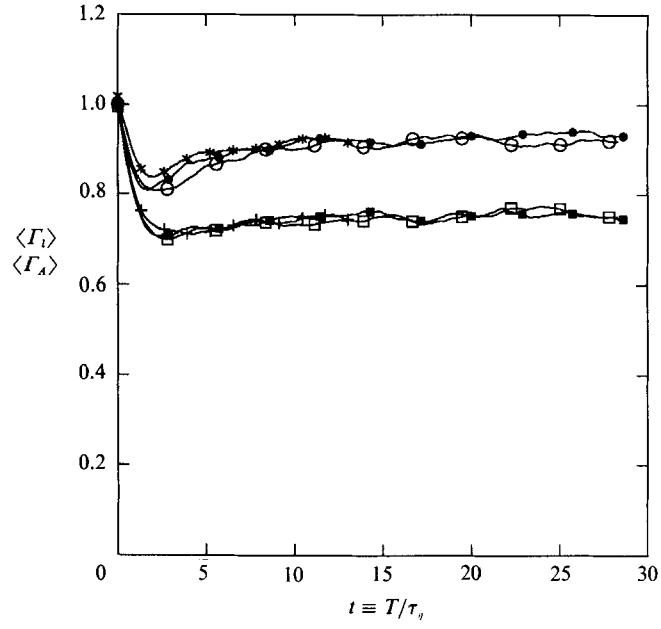

FIGURE 3. Temporal evolution of the mean of the angles. Angle between material-line and maximum positive strain-rate axis, Γ_l: ○, ●, *, for $R_\lambda = 38, 63, 90$. Angle between area-normal and the maximum compressive strain-rate axis, Γ_A: □, ■, +, for $R_\lambda = 38, 63, 90$.

3.1. *Reasons for the smaller mean growth rates*

To understand the reasons for the smaller than estimated mean growth rates we present the ensemble averages of Γ_l and Γ_A calculated from DNS data in figure 3. It may be seen from the figure that the closest alignment between the material line element and the maximum positive strain axis is at about $t = 2$, consistent with the peaking of the growth rates. It may also be seen that the premisses of the previous estimation (Monin & Yaglom 1975) – that there is perfect alignment of line elements with the a_1-direction and area normals with the a_3-direction – are quite erroneous. Perfect alignment corresponds to the angles being zero at steady state: figure 3 indicates that this is not the case. The steady-state values of $\langle \Gamma_l \rangle$ and $\langle \Gamma_A \rangle$ are approximately 0.91 and 0.73 radians respectively.

If the velocity-gradient tensor $\boldsymbol{h}$ is constant in time, (1) has the exact solution

$$l_i(t) = \sum_{b=1}^{3} h'_{ib} C_b \, \mathrm{e}^{k_b t}, \tag{20}$$

where

$$C_b = h'_{bi} l_i(0),$$

and h'_{ib} is the i-component of the eigenvector corresponding to the eigenvalue k_b of $\boldsymbol{h}$. Further, if $\boldsymbol{h}$ is symmetric (i.e. $\boldsymbol{h} = \boldsymbol{s}$), and its eigenvalues are such that $|a_3| \approx a_1$ and $|a_2| \ll a_1$, it can be seen from the above solution (20) that the line element at long times orients itself (almost) completely along the eigenvector corresponding to the maximum positive value. Given this limiting-case behaviour, the reasons for the poor alignment of the line elements with the maximum positive strain-rate axis have to be the effect of the rotation-rate (vorticity), and/or the effect of the non-persistent straining. We now study each of these effects in isolation.

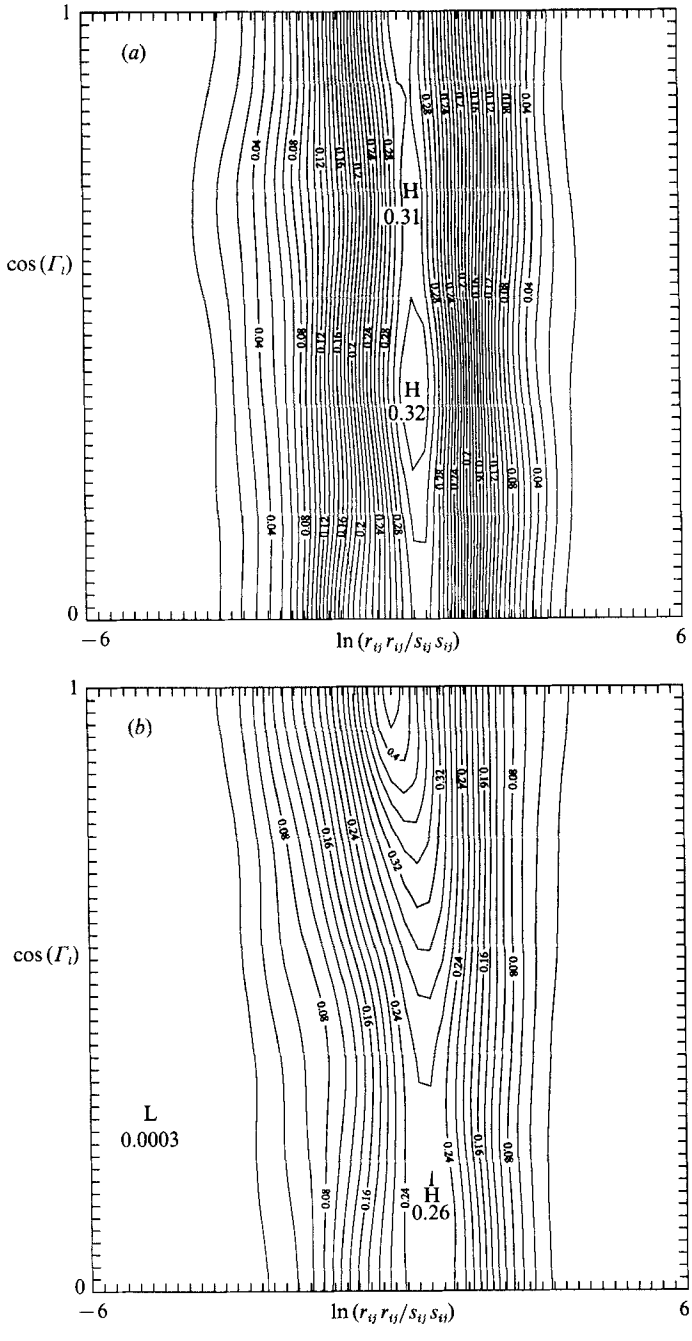

FIGURE 4. Joint p.d.f. of $\ln(r_{ij}r_{ij}/s_{ij}s_{ij})$ and Γ_l: (*a*) $t = 0$; (*b*) $t = 25$.

The effect of vorticity

The effect of rotation rate on $\langle \Gamma_l \rangle$ and $\langle \Gamma_A \rangle$ can be isolated in our computation by holding $\boldsymbol{h}$ constant in time, though varying from particle to particle. So we solve the following modified form of (12):

$$\frac{\mathrm{d}\boldsymbol{B}}{\mathrm{d}t} = \boldsymbol{h}(0)\cdot\boldsymbol{B}(t),$$

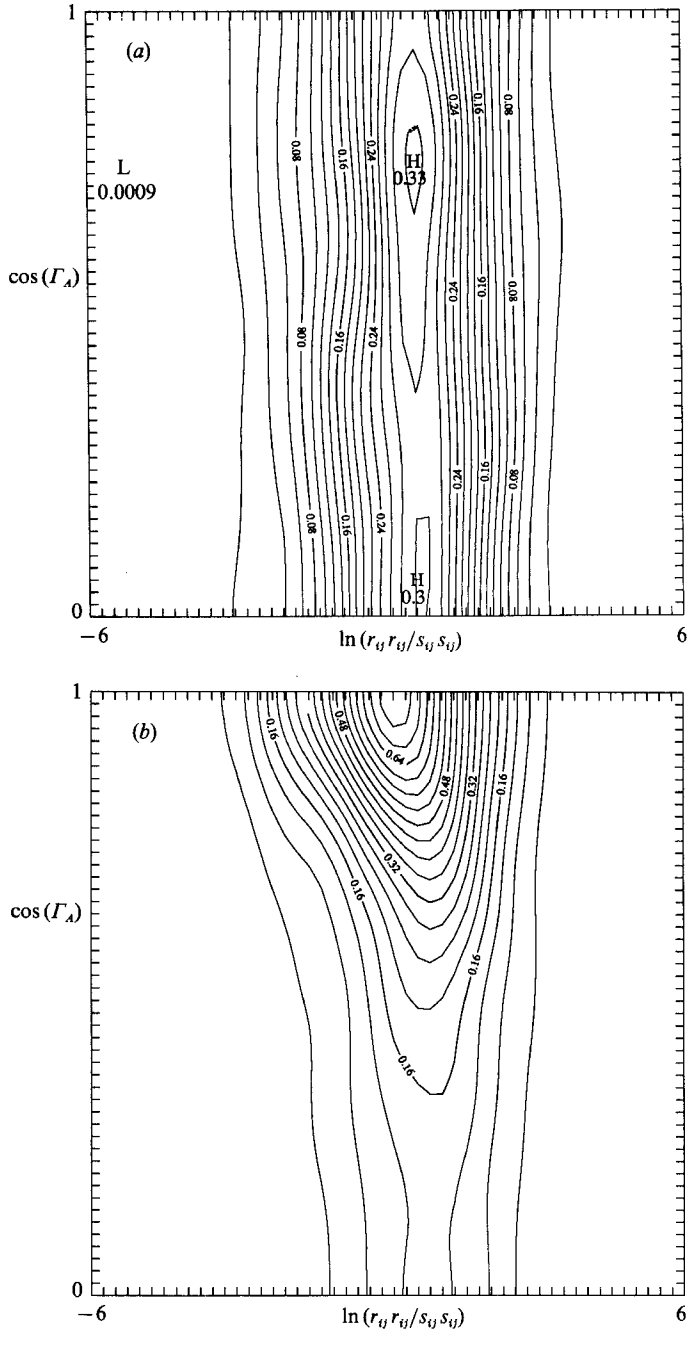

FIGURE 5. Joint p.d.f. of $\ln(r_{ij}r_{ij}/s_{ij}s_{ij})$ and Γ_A: (*a*) $t = 0$; (*b*) $t = 25$.

for an ensemble of particles with $\boldsymbol{h}(0)$ specified from a one-time stationary p.d.f. (obtained from DNS) and the initial $\boldsymbol{l}$ oriented randomly with respect to $\boldsymbol{h}$. This is equivalent to assuming that the integral timescale of $\boldsymbol{h}$ is infinity. Given that the straining is persistent, any deviation of Γ_l and Γ_A from zero would be the effect of vorticity.

In figure 4 the joint p.d.f. of $\ln(r_{ij}r_{ij}/s_{pq}s_{pq})$ and $\cos\Gamma_l$ is presented in the form of

a contour plot. (Initially the material line is uniformly randomly distributed in three dimensions about the a_1-axis. So Γ_l has a spherically symmetric distribution (with $\langle\Gamma_l\rangle \equiv 1$ rad), and $\cos\Gamma_l$ is uniformly distributed in $(0, 1)$. Hence we present the p.d.f.s. of $\cos\Gamma_l$ (and similarly $\cos\Gamma_A$) rather than Γ_l.) Figure 4(*a*) is the joint p.d.f. at time $t = 0$ when the material-line elements are randomly oriented with respect to the $\boldsymbol{h}$-tensor and figure 4(*b*) is the joint p.d.f. at steady state ($t = 25$). Figure 5 presents similar p.d.f.s for Γ_A. At time $t = 0$ the contour lines (in figures 4*a* and 5*a*) are parallel to the y-axis since the initial orientation of the material element with respect to the strain-rate axes is random. The steady-state contours show a high probability of $\cos\Gamma_l$ (and $\cos\Gamma_A$) taking values significantly less than unity even for small values of vorticity. At steady state the contour lines possess a negative slope (less prominent in the case of $\cos\Gamma_l$), indicating that the angles Γ_l and Γ_A increase with the ratio $(r_{ij}r_{ij})/(s_{ij}s_{ij})$. So, it is clear then that even small values of the ratio can cause the material lines to move away from the a_1 direction, which, combined with the high probability of $r_{ij}r_{ij}$ being larger than $s_{ij}s_{ij}$ (≈ 0.45), leads to $\langle\Gamma_l\rangle$ being significantly greater than zero. A similar argument is also valid for $\langle\Gamma_A\rangle$.

The effect of non-persistent straining

In turbulence the principal strain-rate axes change continuously in magnitude and direction. The effect of this on $\langle\Gamma_l\rangle$ and $\langle\Gamma_A\rangle$ can be studied in isolation by modifying (12) to

$$\frac{\mathrm{d}\boldsymbol{B}}{\mathrm{d}t} = \tfrac{1}{2}[\boldsymbol{h}(t) + \boldsymbol{h}^{\mathrm{T}}(t)]\cdot\boldsymbol{B}(t).$$

Since the velocity field that is used to calculate $\boldsymbol{B}$ is symmetric, any deviation of $\langle\Gamma_l\rangle$ and $\langle\Gamma_A\rangle$ from zero will be due only to non-persistent straining.

We solve the above equation for an ensemble of particles with the $\boldsymbol{h}$ time series taken from DNS data. Again the line elements are initially oriented randomly with respect to the strain-rate axes. Figure 6 presents the temporal evolution of the ensemble averages of the angles Γ_l and Γ_A for such a calculation. The steady-state values of $\langle\Gamma_l\rangle$ and $\langle\Gamma_A\rangle$ are approximately 0.78 and 0.60 radians respectively. Although the alignment is better now than in the presence of vorticity (figure 3), the means of the angles are far from zero. It is clear then that non-persistent straining also contributes significantly towards the poor alignment.

Combined effect of vorticity and rotation of the principal axes

Although easily understood in isolation, the effects of the two causes in juxtaposition are difficult to conjecture, for they depend on the relative orientation of the vorticity vector with respect to the axis of rotation of the principal strain-rate directions. For example, a rotation of principal strain-rate directions about the vorticity vector will lead to reduced relative motion between the principal strain axes and the material line element. However, if the principal strain-rate axes rotate in a sense opposite that of vorticity, then we shall have increased relative motion between the line element and the principal directions. In the former case the two effects would (partially) nullify each other, whereas in the latter they would add up. Figure 3 implies that the interaction between vorticity and strain-rate axes rotation in isotropic turbulence is closer to the latter scenario.

3.2. *Reasons for the transient peaks*

Both $\langle\zeta\rangle$ (the growth rate of $\langle\ln l\rangle$) and $\langle\xi\rangle$ (the growth rate of $\langle\ln A\rangle$) exhibit transient peaks (figures 1, 2). Figure 3 shows a dip in the value of $\langle\Gamma_l\rangle$ coincident

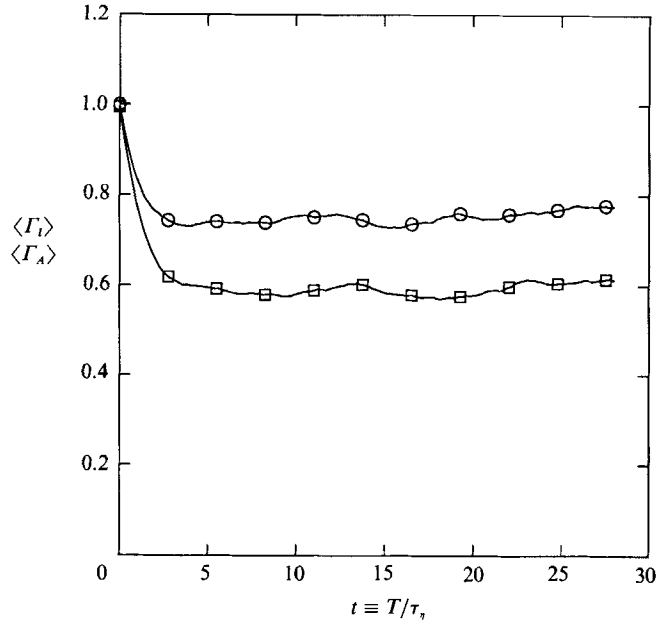

FIGURE 6. Temporal evolution of the mean of the angles for the case of no vorticity: ○, Γ_l; and □, Γ_A.

with the peak in $\langle \zeta \rangle$, whereas no such transient minimum is evident in the case of $\langle \Gamma_A \rangle$. The reason for the peaking of $\langle \xi \rangle$ is not clear, though that for the peaking of $\langle \zeta \rangle$ can be explained with the following simple model similar to the one used by Lumley (1972).

To understand the transient peak of $\langle \zeta \rangle$ (or the transient dip in $\langle \Gamma_l \rangle$) we consider the simplified case in which the velocity-gradient tensor is frozen in time. Although this simplification leads to poor estimates of the mean growth rates, it aids the qualitative understanding of the transient peak. That the non-persistent straining does not contribute significantly towards the transient minimum is evident from the fact that $\langle \Gamma_l \rangle$ exhibits no dip in figure 6. The analysis is further simplified by considering only those line elements whose vorticity vector is oriented close to the intermediate strain-rate axis (a_2-axis). As observed by Ashurst *et al.* (1987) the probability of the occurrence of this event is very high. Referring to figure 7 (*a*) $\boldsymbol{P}$ and $\boldsymbol{C}$ represent the maximum positive and maximum negative strain-rate axes respectively. The only non-zero components of rotation rate are r_{13} and $r_{31} = -r_{13}$. So without loss of generality we can assume that r_{13} is non-negative. We further simplify the model by considering material lines that lie in the $(\boldsymbol{P}, \boldsymbol{C})$-plane. This assumption is not completely necessary but makes possible an analytical solution to the model.

Given the above simplifications, the angle $\langle \Gamma_l \rangle$ between the material line and a_1-axis $\boldsymbol{P}$, evolves according to (recall that $a_1 > 0$ and $a_3 < 0$)

$$\frac{\mathrm{d}\Gamma_l}{\mathrm{d}t} = -\tfrac{1}{2}(a_1 + |a_3|)\sin(2\Gamma_l) + r_{13}. \tag{21}$$

For the case of $r_{13} = 0$ the above equation has the exact solution

$$\tan\Gamma_l(t) = \tan\Gamma_l(0)\,\mathrm{e}^{-(a_1+|a_3|)t}, \tag{22}$$

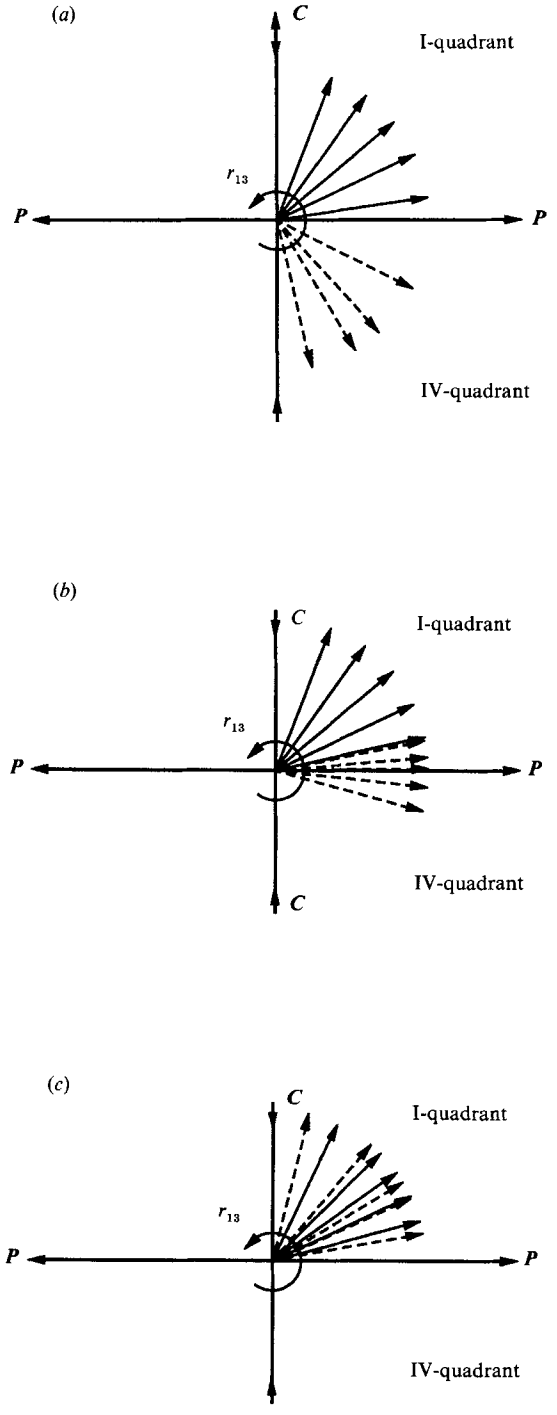

FIGURE 7 (*a–c*). For caption see facing page.

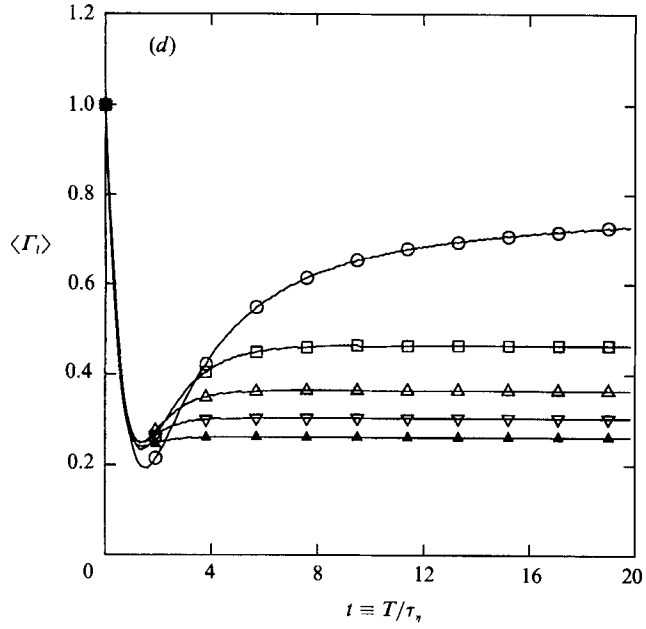

FIGURE 7. Simplified scenarios of line stretching: (*a*) $t = 0$, (*b*) $t \approx 2$, (*c*) steady state. (*d*) $\langle \Gamma_l \rangle$ *vs.* time for $(a_1 + |a_3|)/2r_{13} = \rho = 1.01$ (○), 1.25 (□), 1.50 (△), 1.75 (▽), 2.00 (△).

and for the case of $r_{13} > 0$ the solution is

$$\tan \Gamma_l(t) = \frac{[\tan \Gamma_l(0) - \rho + \delta][\rho - \delta - (\rho + \delta)\, \mathrm{e}^{-r_{13}\delta t}] - 2\delta(\rho - \delta)}{[\tan \Gamma_l(0) - \rho + \delta](1 - \mathrm{e}^{-r_{13}\delta t}) - 2\delta}, \tag{23}$$

where

$$\rho \equiv \frac{a_1 + |a_3|}{2r_{13}}, \quad \delta \equiv (\rho^2 - 1)^{\frac{1}{2}},$$

and $\Gamma_l(0)$ is the initial value.

Case (*a*): $r_{13} = 0$. From the above definitions and (22) it can be seen that $\Gamma_l(t)$ decays exponentially to zero from its initial value. Since $|\Gamma_l|$ decreases monotonically these material lines cannot cause the transient dip.

Case (*b*): $r_{13} > \frac{1}{2}(a_1 + |a_3|) > 0$. In this case δ is imaginary and the exponentials in (23) become sine and cosine functions. For such a line Γ_l is a periodic function. Such material lines do not contribute towards the transient dip either.

Case (*c*): $0 < r_{13} < \frac{1}{2}(a_1 + |a_3|)$. In this case δ is real and positive and the exponentials in (23) decay as t increases. At long times Γ_l tends to an asymptotic value Γ_l^*. The material lines that fall in this category cause the transient dip and are now studied in further detail.

A pictorial depiction of the evolution of $\langle \Gamma_l \rangle$ for lines with ρ greater than unity is presented in figure 7. Figure 7(*a*) represents the initial condition. The material-line elements are oriented randomly with respect to the principal strain-rate axes (which corresponds to $\langle \Gamma_l \rangle \equiv 1$ rad). Because of the arbitrary choice of the sign of the unit vectors $\boldsymbol{P}$ and $\boldsymbol{C}$ all material lines can be placed in the I- or the IV-quadrants. Initially the line elements are distributed equally between the I- and IV-quadrants.

In the I-quadrant sin $(2\Gamma_l)$ is positive and the material lines move towards their steady-state location at an angle defined by

$$\Gamma_l^* \equiv \tfrac{1}{2} \sin^{-1} (1/\rho). \tag{24}$$

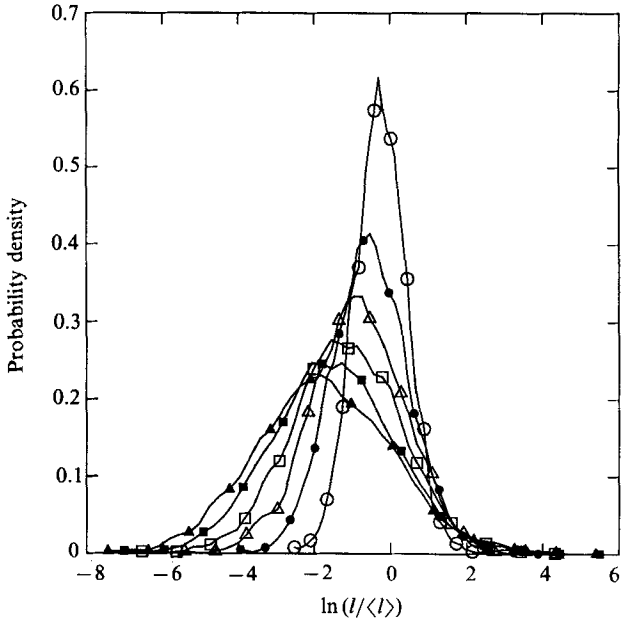

FIGURE 8. P.d.f. of $\ln(l/\langle l\rangle)$ *vs.* time: ○, ●, △, □, ■, ▲, correspond to $t = 5, 10, 15, 20, 25, 30$.

At this angle the effect of vorticity is completely balanced by that of strain rate.

In the IV-quadrant $\sin(2\Gamma_l)$ is negative and hence $\mathrm{d}\Gamma_l/\mathrm{d}t$ is positive. Vorticity and straining work together to improve the alignment. The line elements move toward the a_1-axis ($\boldsymbol{P}$) and cross over to the I-quadrant. During this transition period ($t \approx 2$) most elements originating from the IV-quadrant are close to the a_1-axis after which they settle down in the I-quadrant at angles dictated by (24). It is during the cross-over (figure 7*b*) that the alignment is at its best and consequently the growth rate at its peak.

At steady state (figure 7*c*) all the line elements are situated in the I-quadrant at various angles depending on the magnitude of vorticity relative to strain rate, (24).

Quantitative results of the model are provided in figure 7(*d*). The solution (23) to the evolution equation of Γ_l, (21), is completely characterized by ρ and r_{13}. In fact r_{13} only determines the timescale and is not important in the study of the transient dip of $\langle\Gamma_l\rangle$. In figure 7(*d*) we present the ensemble average of Γ_l calculated using (23) with a random spherical distribution of $\Gamma_l(0)$ (i.e. $\cos\Gamma_l(0)$ distributed uniformly in $(0, 1)$). The results are presented for various values of ρ (> 1.0) with r_{13} held at unity. The transient dip in $\langle\Gamma_l\rangle$ is evident for all ρ-values less than 1.5. For higher values of ρ the effect of strain is too large for the overshoot of the angle Γ_l.

4. Steady-state distributions of $\ln l$ and $\ln A$

The objective of this section is to characterize the p.d.f. of $l(t)$ and $A(t)$ (or some function thereof) at steady state.

In homogeneous, isotropic turbulence, Batchelor (1952) reasons that, if *the influence of the initial length has been removed by letting, in effect,* $e(0) \to 0$, *there is no length other than* $\langle e(t)\rangle$ *on which the statistical properties can depend, and a similarity in the shape of the probability density function of* $e(t)$ *at different values of* t *seems*

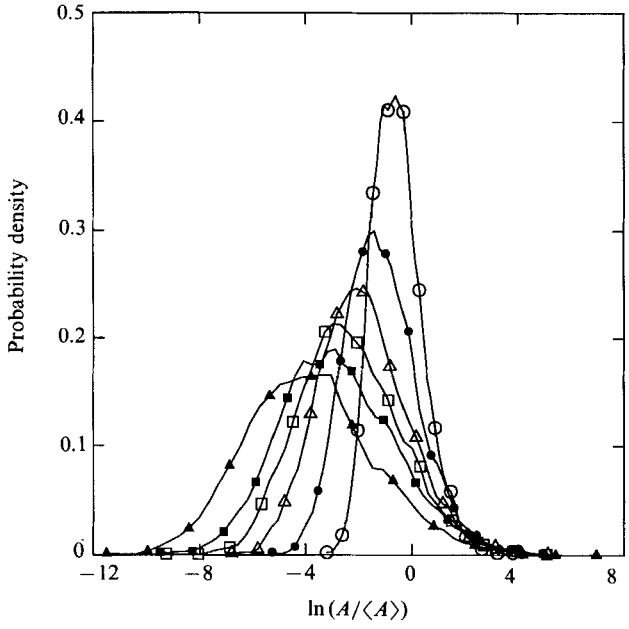

FIGURE 9. P.d.f. of $\ln(A/\langle A\rangle)$ *vs.* time: legend as for figure 8.

inevitable. In other words, it seems that $e(t)/\langle e(t)\rangle$ *is a stationary random function.* A similar argument for area elements implies that the p.d.f. of $f/\langle f\rangle$ is stationary at steady state. (Note that $e(t)/\langle e(t)\rangle \equiv l/\langle l\rangle$ and $f(t)/\langle f(t)\rangle \equiv A/\langle A\rangle$.)

The DNS data again make possible a direct test of the above hypotheses. In figures 8 and 9 the p.d.f.s of $\ln(l/\langle l\rangle)$ and $\ln(A/\langle A\rangle)$ are plotted for various times. If the hypothesis is correct, these two p.d.f.s attain stationarity at steady state and it may be seen from the figures that such is not the case. (Note that stationarity of $(l/\langle l\rangle)$ implies the stationarity of $\ln(l/\langle l\rangle)$ because the relationship between the two p.d.f.s is independent of time.)

The medians of the p.d.f.s are negative, indicating that $l(t)$ and $A(t)$ values of most material elements are smaller than the mean and those of a few elements are much larger than the mean. With time the median values get progressively smaller with fewer and fewer particles determining the higher moments of the distribution. In figure 10 we present the evolution in time of $(\ln A/\langle A\rangle)^n$ for $n = 1$, 2 and 3. Despite the large statistical errors in calculating these quantities, figure 10 is evidence that the moments increase with time.

4.1. *Why is* $l/\langle l\rangle$ *not a stationary random variable?*

It can be shown analytically that if the variance and the integral timescale of ζ (the rate of change of $\ln l$) are non-zero, then $l/\langle l\rangle$ cannot be statistically stationary. The extent of the departure from stationarity is proportional to the product of the variance and the integral timescale.

The proof entails analysing the p.d.f.s of the random variables $\ln l$ (or $\ln A$) which evolve according to (9) and (10). As pointed earlier, the stationarity of $l/\langle l\rangle$ implies the stationarity of the random variable $\ln(l/\langle l\rangle)$. So, conversely, if it can be shown that any moment of $\ln(l/\langle l\rangle)$ grows in time, then the random variable $l/\langle l\rangle$ cannot be stationary.

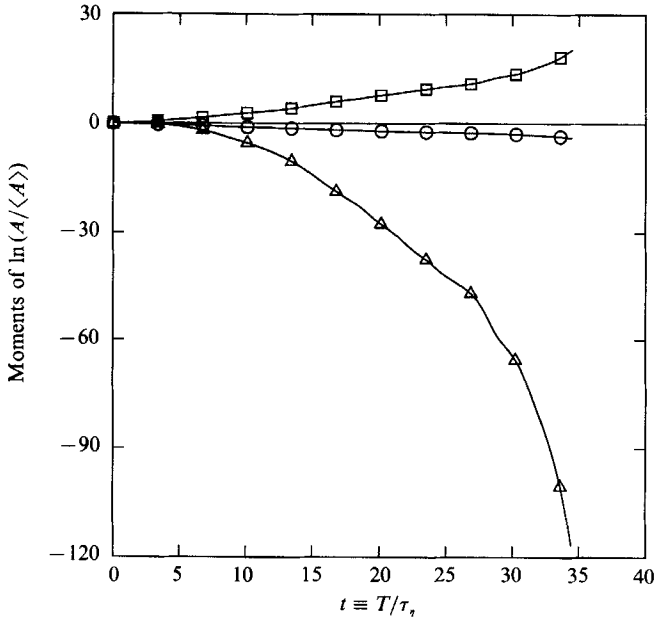

FIGURE 10. Temporal evolution of the raw moments of $\ln A/\langle A\rangle$: ○, □, △ correspond to first, second and third moments.

In particular, we consider the variance of $\ln(l/\langle l\rangle)$. It is trivial to show that

$$\mathrm{var}(\ln l/\langle l\rangle) = \mathrm{var}(\ln l) = \mathrm{var}(\ln l - \langle \ln l\rangle).$$

Starting from (9) the evolution equation for the variance of $\ln l$ can be derived:

$$\frac{\mathrm{d}}{\mathrm{d}t}\mathrm{var}(\ln l - \langle \ln l\rangle) = 2\langle(\ln l(t) - \langle \ln l(t)\rangle)(\zeta(t) - \langle\zeta(t)\rangle)\rangle$$

$$= 2\left\langle \int_0^t (\zeta(t') - \langle\zeta(t')\rangle)(\zeta(t) - \langle\zeta(t)\rangle)\,\mathrm{d}t' \right\rangle.$$

At steady state (i.e. when $t \gg T_\zeta$, the integral timescale of ζ, which is non-dimensional since it is the integral timescale in normalized time) we can write

$$\frac{\mathrm{d}}{\mathrm{d}t}\mathrm{var}(\ln l - \langle \ln l\rangle) = 2\,\mathrm{var}(\zeta)\,T_\zeta. \tag{25}$$

Similarly, for area elements we have

$$\frac{\mathrm{d}}{\mathrm{d}t}\mathrm{var}(\ln A - \langle \ln A\rangle) = 2\,\mathrm{var}(\xi)\,T_\xi, \tag{26}$$

where T_ξ is the integral timescale of ζ. Non-zero values of the variance and integral timescale of ζ would indicate a linear growth of the variance of $\ln l/\langle l\rangle$, and consequently $l/\langle l\rangle$ could not be stationary random variable. A similar argument is valid for the non-stationarity of $A/\langle A\rangle$.

Although it is clear that the variances of ζ and ξ are strictly positive, it cannot be shown by analytical means alone that their integral timescales are non-zero. Consequently we appeal to the DNS data. The steady-state p.d.f.s computed from

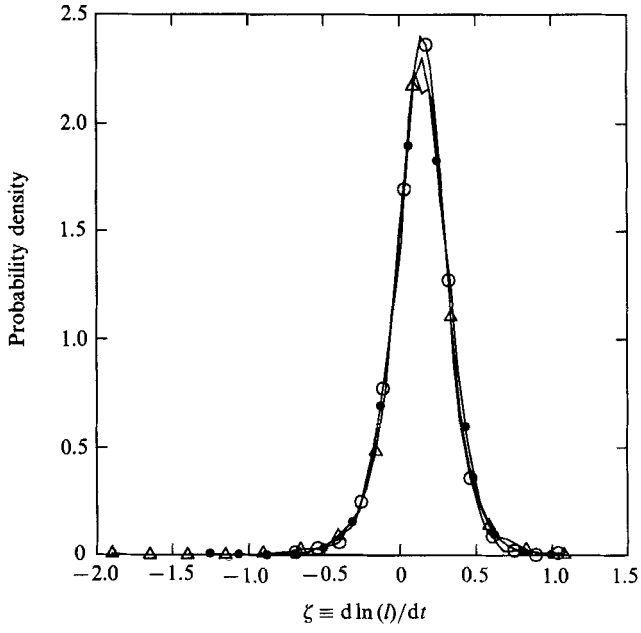

FIGURE 11. P.d.f. of the growth rate of $\ln l$, ζ, at steady state: ○, ●, △, correspond to $R_\lambda = 38, 63, 90$.

DNS data of ζ and ξ are shown in figures 11 and 12 and their autocorrelations in figure 13. (The autocorrelation of ξ was also given in Yeung *et al.* 1990.) The autocorrelations provided are the biased versions so that we have minimal statistical error at large time lags. Clearly the integral timescales are non-zero. The growth rates of the variances of $\ln l$ and $\ln A$ are provided in table 2.

4.2. *Implications of the central limit theorem*

It was seen in §1.1 that the growth rates of $\ln l$, (ζ), and of $\ln A$, (ξ), are statistically stationary at steady state. The behaviour of the integral of a statistically stationary random variable is discussed in Tennekes & Lumley (1975) and our discussion proceeds along similar lines. Each of $\ln l$ and $\ln A$ can be viewed as a sum of identically distributed random variables, i.e. as the integrals of ζ and ξ. The central limit theorem governs the behaviour of the probability distribution of the sum of a large number of independent, identically distributed random variables under suitable conditions. Since ζ and ξ are continuous and differentiable their integrals cannot be regarded as the sum of independent variables. However, if the integration is performed over times much larger than the timescale of ζ (or ξ), the probability distribution of the integral can be expected to be amenable to the central limit theorem. Hence the p.d.f. of $\ln l$ (and $\ln A$) at large times can be expected to tend to Gaussian. Since a Gaussian distribution is completely characterized by its mean and standard deviation, the standardized variables

$$\hat{l} = (\ln l - \langle \ln l \rangle)/[\mathrm{var}\,(\ln l)]^{\frac{1}{2}} \tag{27}$$

and

$$\hat{A} = (\ln A - \langle \ln A \rangle)/[\mathrm{var}\,(\ln A)]^{\frac{1}{2}}, \tag{28}$$

can be expected to be statistically stationary. Recall that Kraichnan (1974) shows that l and A are log-normally distributed for the case of a white-noise velocity field.

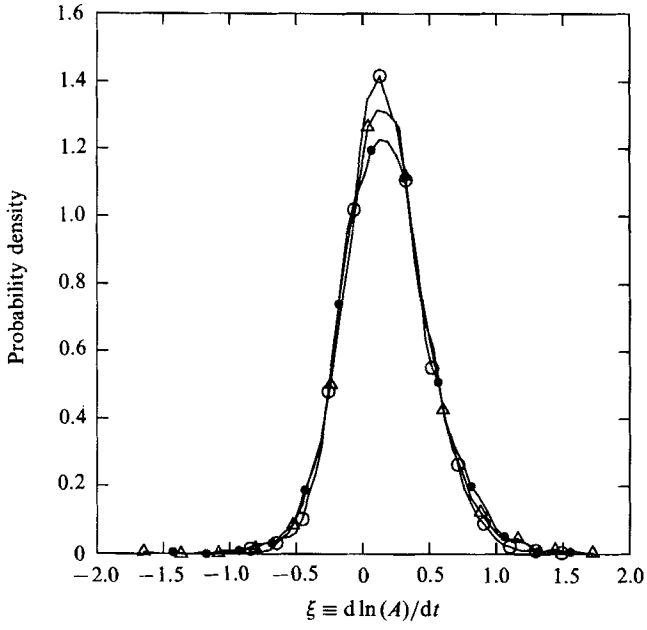

FIGURE 12. P.d.f. of the growth rate of $\ln A$, ξ, at steady state: legend as for figure 11.

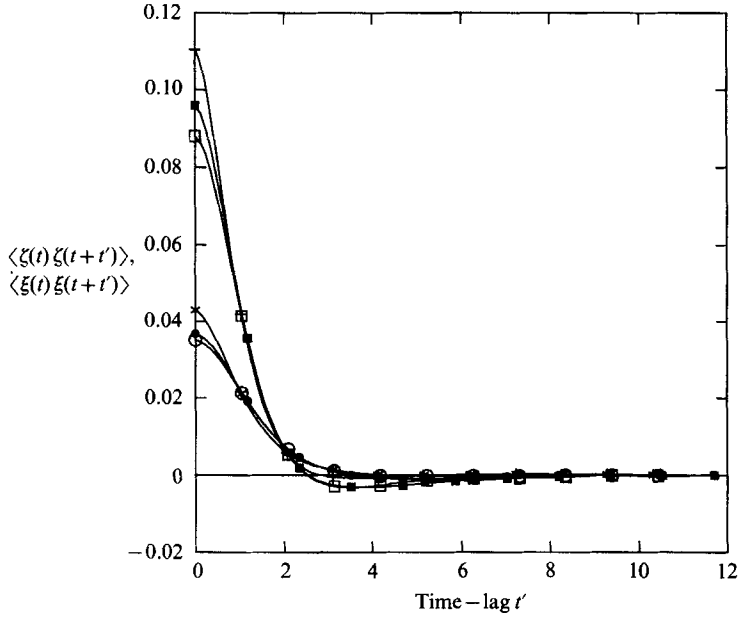

FIGURE 13. Autocovariance of the growth rate of $\ln l$, ζ: ○, $R_\lambda = 38$, $T_\zeta \mathrm{var}(\zeta) = 0.0491$; ●, $R_\lambda = 63$, $T_\zeta \mathrm{var}(\zeta) = 0.0488$; *, $R_\lambda = 90$, $T_\zeta \mathrm{var}(\zeta) = 0.0528$. Autocovariance of the growth rate of $\ln A$, ξ: □, $R_\lambda = 38$, $T_\xi \mathrm{var}(\xi) = 0.0892$; ■, $R_\lambda = 63$, $T_\xi \mathrm{var}(\xi) = 0.0945$; +, $R_\lambda = 90$, $T_\xi \mathrm{var}(\xi) = 0.104$.

4.3. *Stationarity of the standardized random variables*

In figures 14 and 15 the evolution of the p.d.f.s of $\hat{l}$ and $\hat{A}$ are shown. Clearly the p.d.f.s do attain self-similarity to within statistical error. The first few moments of $\hat{l}$ and $\hat{A}$ (for the $R_\lambda = 38$ case) are shown in figures 16 and 17 respectively. It can be

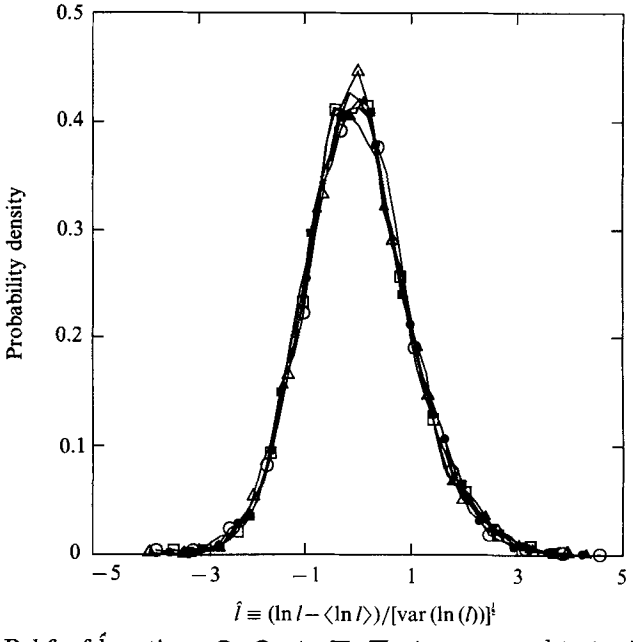

FIGURE 14. P.d.f. of $\hat{l}$ *vs.* time: ○, ●, △, □, ■, ▲ correspond to $t = 5, 10, 15, 20, 25, 30$.

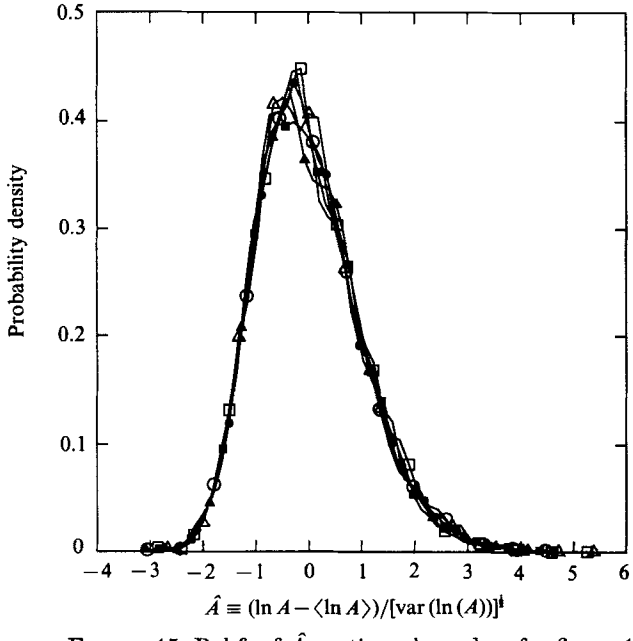

FIGURE 15. P.d.f. of $\hat{A}$ *vs.* time: legend as for figure 14.

seen that to within statistical error the moments are constant at steady state. The stationary values for all the moments of $\hat{l}$ and the third, fourth and sixth moments of $\hat{A}$ are quite close to the corresponding standard Gaussian values. (The third, fourth, fifth and sixth moments of a standard normal random variable are 0, 3, 0 and 15 respectively.) The fifth moment of $\hat{A}$ is approximately 3 and it is not clear if this deviation from the standard normal value is due to statistical error alone. In any case

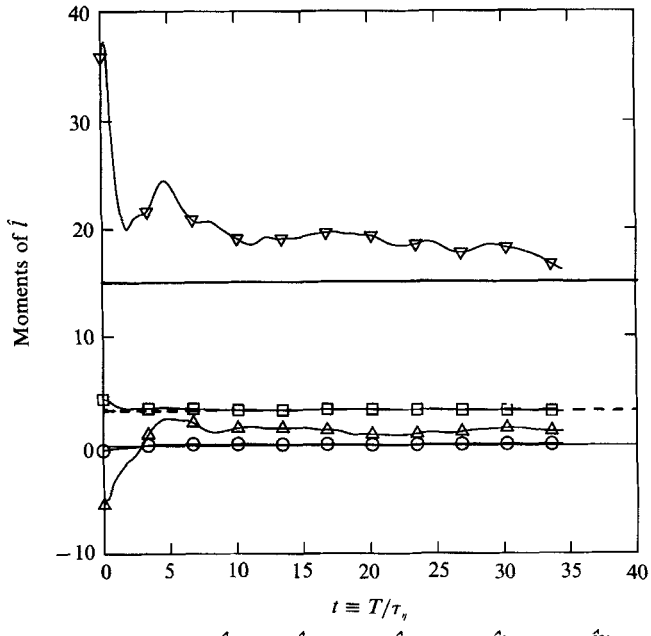

FIGURE 16. Moments of $\hat{l}$: ○, $\langle \hat{l}^3 \rangle$; □, $\langle \hat{l}^4 \rangle$; △, $\langle \hat{l}^5 \rangle$; ▽, $\langle \hat{l}^6 \rangle$ of DNS data. ---, $\langle \hat{l}^4 \rangle$ and ——, $\langle \hat{l}^6 \rangle$ of a standard Gaussian distribution.

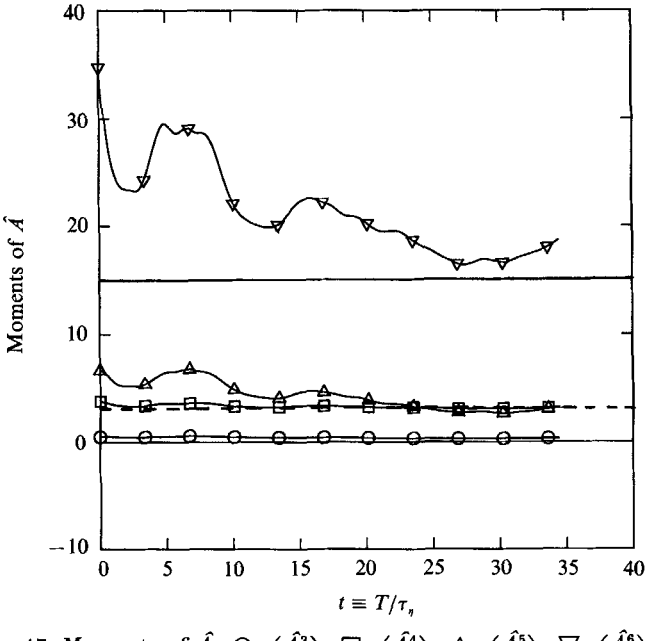

FIGURE 17. Moments of $\hat{A}$: ○, $\langle \hat{A}^3 \rangle$; □, $\langle \hat{A}^4 \rangle$; △, $\langle \hat{A}^5 \rangle$; ▽, $\langle \hat{A}^6 \rangle$ of DNS data. ---, $\langle \hat{A}^4 \rangle$ and ——, $\langle \hat{A}^6 \rangle$ of a standard Gaussian distribution.

it is clear that the central limit theorem comes quite close to predicting the p.d.f.s of $\ln l$ and $\ln A$ correctly. The steady-state p.d.f.s of $\hat{l}$ and $\hat{A}$ for various Reynolds numbers are presented in figures 18 and 19 and there is very little variation (to within statistical error).

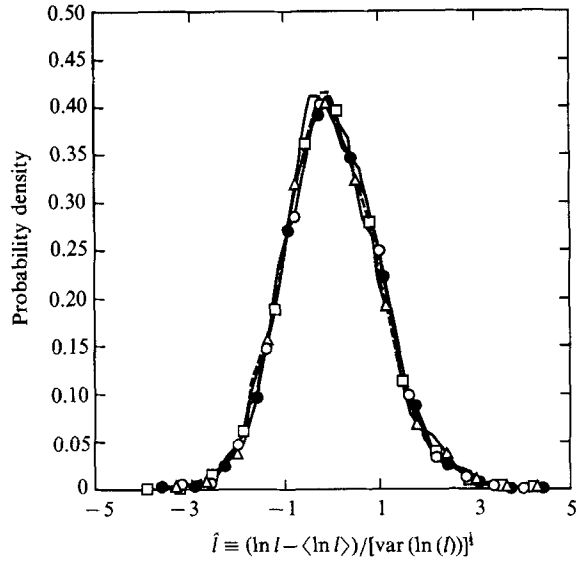

FIGURE 18. Steady-state p.d.f. of $\hat{l}$ for various R_λ: ○, ●, △ correspond to $R_\lambda = 38, 63, 90$ of DNS. □ and the dashed line represent $R_\lambda = 38$ of the model.

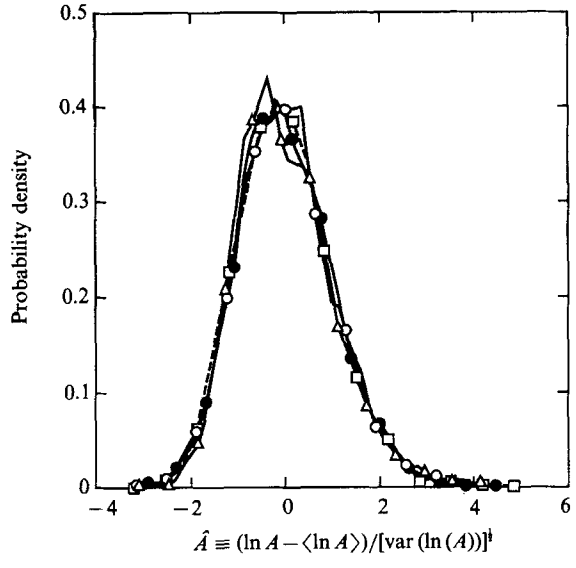

FIGURE 19. Steady-state p.d.f. of $\hat{A}$ for various R_λ: legend as for figure 18.

In this section it has been established that: at steady state the mean and variance of $\ln l$ and $\ln A$ grow at constant rates that are only weakly dependent on Reynolds number (see table 2 for exact values); and the p.d.f.s of the parameters $\hat{l}$ and $\hat{A}$, scaled to account for the growth of mean and variance only, attain stationary forms that appear independent of Reynolds number.

The fact that, when standardized, $\ln l$ attains stationarity implies that there are two lengthscales in the problem: $e(0)\exp(\langle\zeta\rangle t)$ and $e(0)\exp[(T_\zeta^2\,\mathrm{var}\,(\zeta)t)^{\frac{1}{3}}]$. As can be seen from the previous subsection the second lengthscale indicates the extent of the deviation of $l/\langle l\rangle$ from stationarity. In other words, this lengthscale indicates the

extent to which the moments of l are in excess of what can be accounted for by the growth of $\langle l \rangle$ alone. The ratio $(T_\zeta \operatorname{var} \zeta)^{\frac{1}{2}}/\langle \zeta \rangle$ is larger than unity (as can be seen from table 2) indicating that $l/\langle l \rangle$ is far from stationary at steady state. Similar arguments are valid for $A/\langle A \rangle$.

5. Deformation of a volume element

In this section the statistics of quantities that characterize material volume-element deformation are discussed. The quantities of interest are θ (the angle between two material lines that are initially orthogonal) and α (the angle between a material-plane normal and a material line that is initially normal to the plane) and the eigenvalues of the Cauchy–Green tensor $\boldsymbol{W}$ of material element deformation (see §1.2 for definitions). Since the sign of the direction of the material lines are arbitrary, we deal with the absolute values of the angles.

The statistics of the evolution of $\ln \sin|\theta|$ and $\ln \cos|\alpha|$ are completely determined by the statistics of ζ and ξ. For, referring to (15), we have

$$\ln \sin|\theta| = \ln A - \ln l_1 - \ln l_2.$$

Taking means and recognizing that l_1 and l_2 are statistically equivalent we have

$$\frac{\mathrm{d}}{\mathrm{d}t}\langle \ln \sin|\theta| \rangle = \langle \xi \rangle - 2\langle \zeta \rangle \approx -0.105 \text{ (at steady state)}. \tag{29}$$

Similarly, referring to (16), we obtain

$$\frac{\mathrm{d}}{\mathrm{d}t}\langle \ln \cos|\alpha| \rangle = -[\langle \xi \rangle + \langle \zeta \rangle] \approx -0.300 \text{ (at steady state)}. \tag{30}$$

So two material lines that are initially orthogonal, on average, become colinear at the exponential rate given by (29). Similarly a material line that is initially normal to a material plane becomes coplanar at the much faster rate given by (30).

An infinitesimal material sphere deforms under the influence of straining into an ellipsoid. The Cauchy–Green tensor $\boldsymbol{W}$ describes this deformation. The principal axes of the ellipsoid are given by $(w_1)^{\frac{1}{2}}$, $(w_2)^{\frac{1}{2}}$ and $(w_3)^{\frac{1}{2}}$ relative to the initial diameter of the sphere, where, $w_1 \geqslant w_2 \geqslant w_3$ are the eigenvalues of $\boldsymbol{W}$. Given that $\boldsymbol{B}(0) = \boldsymbol{I}$, the initial values of all the eigenvalues are unity. Further, since the fluid is incompressible the material ellipsoid conserves volume and hence $w_1 w_2 w_3 = 1$. It is clear then that $w_1 \geqslant 1$ and $w_3 \leqslant 1$. However, the behaviour of w_2 is not clear.

In figure 20(*a*) the evolution of the logarithm of the eigenvalues is plotted for various Reynolds numbers. Not surprisingly, there is not much difference between the various Reynolds numbers. The mean of $\ln w_2$ is positive and much smaller in magnitude than the means of $\ln w_1$ and $\ln w_3$. The relative magnitude of $\ln w_2$ with respect to that of $\ln w_1$ and $\ln w_3$ is still not clear. From the ordering of the eigenvalues ($\ln w_1 \geqslant \ln w_2 \geqslant \ln w_3$) and incompressibility condition ($\ln w_1 + \ln w_2 + \ln w_3 = 0$) we know the following:

(i) Once $\ln w_1$ and $\ln w_2$ are known $\ln w_3$ can be calculated. Hence the joint p.d.f. of $\ln w_1$ and $\ln w_2$ contains all the one-time statistical information about the eigenvalues of $\boldsymbol{W}$.

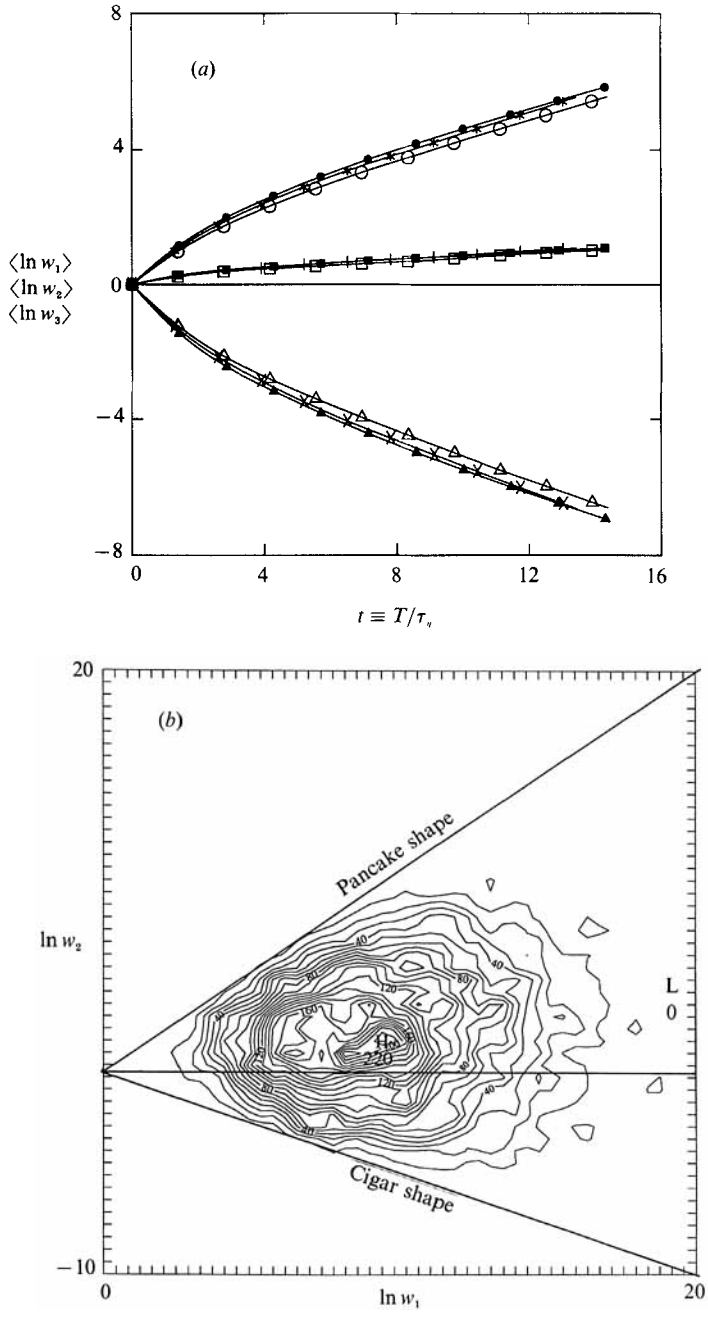

FIGURE 20. Evolution of Cauchy–Green tensor: (*a*) ○, $\langle \ln w_1 \rangle$; □, $\langle \ln w_2 \rangle$; △, $\langle \ln w_3 \rangle$, for $R_\lambda = 38$; ●, ■, ▲ respectively for $R_\lambda = 63$; *, +, × respectively for $R_\lambda = 90$. (*b*) Joint p.d.f. of $\ln w_1 - \ln w_2$ at $t = 30$.

(ii) The maximum value that $\ln w_2$ can take is $\ln w_1$. This case corresponds to the initial infinitesimal material sphere deforming to a *pancake* shape.

(iii) The minimum value that $\ln w_2$ can take is $-\frac{1}{2}\ln w_1$. This represents the case when the material sphere deforms to a *cigar* shape.

	$\langle \ln w_1 \rangle$	$\langle \ln w_2 \rangle$	$\langle \ln w_3 \rangle$
DNS value	0.28	0.04	−0.32
Estimate of (32)–(34)	0.27	0.06	−0.33
Estimate of (31)	0.80	0.20	−1.00

TABLE 3. Comparison of the estimates and DNS values of the eigenvalues of $\boldsymbol{W}$

In figure 20(*b*) the joint p.d.f. of $\ln w_1$ and $\ln w_2$ calculated from DNS data at $t = 30$ is provided. Clearly the joint p.d.f. is a function of time. It is found that the qualitative details of the joint p.d.f.s at $t = 5$, 10, 15, 25 (not shown) vary very little from that of the joint p.d.f. at $t = 30$. The joint p.d.f. indicates that the cigar shape and the pancake shape are equally probable. However, the event $\{\ln w_2 \approx 0^+\}$ is about five times as probable as either the cigar case or the pancake case. (This estimate is obtained from the p.d.f. of $\ln w_2$ at time $t = 30$ (not shown).) So with a high probability an initially spherical volume of fluid deforms into an ellipsoid with one axis (w_1) elongated, one axis (w_2) changing little, and the third (w_3) shrinking to conserve the volume. In case of some (25%) of the material elements $\ln w_2$ is negative.

For the ideal case of no vorticity and persistent straining, the evolution of the eigenvalues is easy to compute. From (19) we can derive

$$\frac{\mathrm{d}}{\mathrm{d}t}\langle \ln w_i \rangle \approx 2\langle a_i \rangle. \tag{31}$$

However, from previous sections it is known that estimates obtained by neglecting the effects of vorticity and non-persistent straining are incorrect by over 200%. So the following estimates for the steady-state growth rates of the logarithm of eigenvalues may be expected to be better:

$$\frac{\mathrm{d}}{\mathrm{d}t}\langle \ln w_1 \rangle \approx 2\langle \zeta \rangle, \tag{32}$$

$$\frac{\mathrm{d}}{\mathrm{d}t}\langle \ln w_3 \rangle \approx -2\langle \xi \rangle, \tag{33}$$

$$\frac{\mathrm{d}}{\mathrm{d}t}\langle \ln w_2 \rangle \approx 2[\langle \xi \rangle - \langle \zeta \rangle]. \tag{34}$$

The steady-state growth rates of $\ln w_1$, $\ln w_2$ and $\ln w_3$ calculated from figure 20 are approximately 0.28, 0.04 and −0.32 respectively. These values are very close to the estimates of (32)–(34) as shown in table 3.

6. Performance of the stochastic model

The stochastic model of Girimaji & Pope (1990) is a tensor-valued diffusion process for the velocity gradients. The modelled Lagrangian velocity gradients mimic the DNS velocity gradients and can to be used as a substitute in the study of material-element deformation. The model velocity-gradient time series satisfies the pertinent

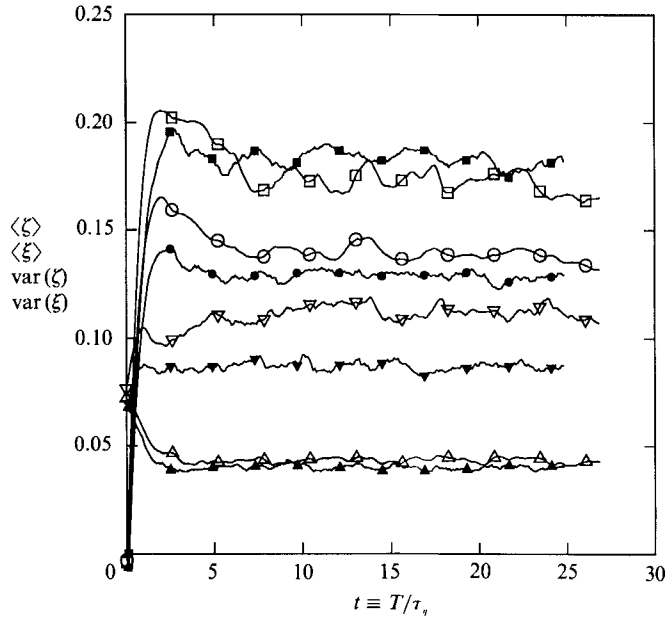

FIGURE 21. Comparison of the statistics of ζ and ξ from DNS and the stochastic model: ○, $\langle\zeta\rangle$; □, $\langle\xi\rangle$; △, var(ζ); ▽, var(ξ) of DNS for the $R_\lambda = 90$ case. Filled symbols represent the corresponding model quantities.

incompressibility, homogeneity and isotropy constraints exactly. The drift and the diffusion terms of the diffusion process are such that at least the first few moments of the modelled velocity-gradient distribution are close to those computed from DNS data.

In this section the diffusion model is tested for its performance in calculating the details of material-line and surface-element evolution. Having already established that the details are Reynolds-number independent we do not make a detailed Reynolds-number dependence study of the comparison of the model and DNS calculations.

The performance of the model is compared to that of DNS for the following aspects of material element deformation: (i) one-time p.d.f. of ζ and ξ; (ii) two-time autocorrelations of ζ and ξ; (iii) the p.d.f.s of $\hat{l}$ and $\hat{A}$ at steady state; (iv) the material volume deformation quantities.

One-time p.d.f. of ζ and ξ

The one-time p.d.f.s of ζ and ξ are important since the means determine the growth rate of the means of $\ln l$ and $\ln A$, and the variance plays an important role in determining the growth rates of the variance of $\ln l$ and $\ln A$. In figure 21 the temporal evolutions of means and variances (of ζ and ξ) of the model and DNS are compared for the $R_\lambda = 90$ case. A similar comparison is made for the $R_\lambda = 38$ case in Girimaji & Pope (1990). The agreement in both the cases is good.

Two-time correlations of ζ and ξ

The two-time correlations are important since they determine the integral lengthscales which, along with the variances, determine the growth rate of the variance of $\ln l$ and $\ln A$ ((25) and (26)). In figure 22 we compare the two-time

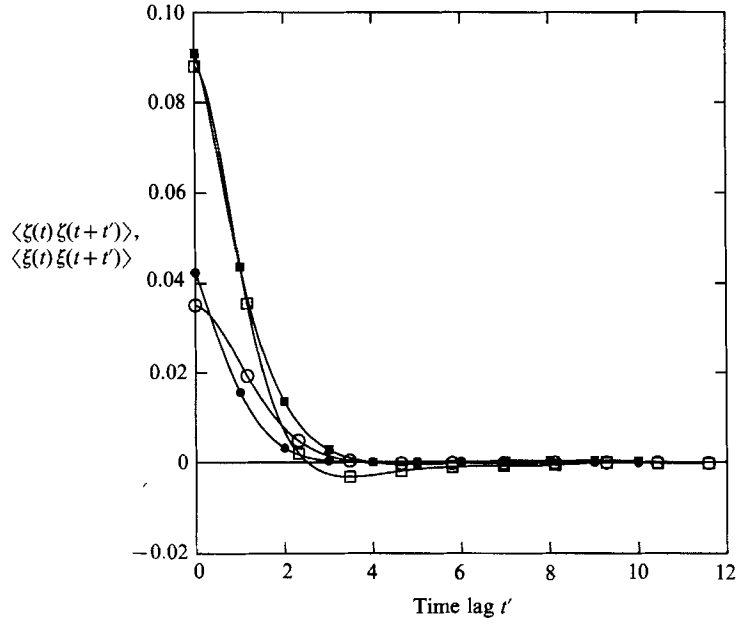

FIGURE 22. DNS *vs.* model. Autocovariances of ζ and ξ for $R_\lambda = 90$: ○, DNS, ζ, $T_\zeta \mathrm{var}(\zeta) = 0.0490$; ●, model, ζ, $T_\zeta \mathrm{var}(\zeta) = 0.0407$; □, DNS, ξ, $T_\xi \mathrm{var}(\xi) = 0.0892$; ■, model, ξ, $T_\xi \mathrm{var}(\xi) = 0.108$.

covariances. The model integral timescale is lower by about 17 % for ζ and higher by 17 % for ξ. Though the disagreement is not much, it is large considering the very good agreement between the model and the DNS for the case of two-time strain-rate correlations in Girimaji & Pope (1990). However, as can be seen from (9) and (10) the relative orientation of the material element with the principal strain axes also plays a role in determining ζ and ξ. The orientation of the material element is affected by the rotation-rate tensor, the two-time correlation of which is poorly replicated by the model. It is to this shortcoming of the model that we attribute the relatively poor estimation of the integral timescales.

Steady-state p.d.f.s of $\hat{l}$ and $\hat{A}$

After removing the effects of the growing mean and variance of $\ln l$ and $\ln A$ by suitable scaling, it was shown in §4 that the scaled parameters $\hat{l}$ and $\hat{A}$ attain statistical stationarity. If the probability distributions of $\hat{l}$ and $\hat{A}$ computed from the model are also governed by the central limit theorem then it is inevitable that the model p.d.f.s should match the corresponding ones calculated from DNS. In figure 18 the steady-state p.d.f. of $\hat{l}$ of the model is compared to that of DNS. In figure 19 a similar comparison is made for $\hat{A}$. (Note that the model $\hat{l}$ and $\hat{A}$ are scaled using the model values of mean and variance.) The agreement is quite good.

Material volume deformation quantities

As seen before, the statistics of the angles θ and α are completely determined by the statistics of the random variables ζ and ξ. It was shown in figure 21 that the first two moments of these random variables are calculated fairly accurately by the model. It can be inferred then that the model does well in calculating the angles. Clearly the estimates of (32)–(34) are also valid for the eigenvalues calculated from the model. The evolution of the eigenvalues are compared in figure 23. The

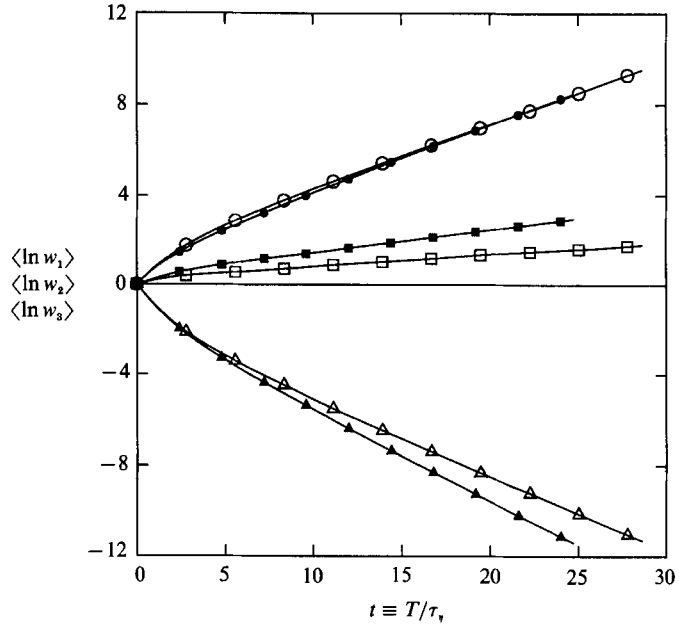

FIGURE 23. DNS *vs.* model. Evolution of Cauchy–Green tensors: ○, $\langle \ln w_1 \rangle$; □, $\langle \ln w_2 \rangle$; △, $\langle \ln w_3 \rangle$, DNS data for the $R_\lambda = 38$ case. Filled symbols represent the corresponding model calculations.

agreement is very good in the case of w_1. The model predicts a faster decrease of $\langle \ln w_3 \rangle$ than DNS. This is consistent with the model overestimation of $\langle \xi \rangle$ (see figure 21 and (33)). The overestimation of the decay rate of $\langle \ln w_3 \rangle$ by the model is coupled with its overestimation of the growth rate of $\langle \ln w_2 \rangle$.

7. Summary and conclusions

In this work we analyse the evolution of material line, surface and volume elements using velocity-gradient data generated by DNS. The diffusive nature of turbulence renders the study of finite lines and surfaces computationally expensive. So we study the evolution of incontiguous infinitesimal material-line ($\boldsymbol{e}(t)$) and material-area ($\boldsymbol{f}(t)$) elements. Over each such infinitesimal element the strain rate is uniform and hence we need only one-point velocity-gradient information following fluid particles. Using DNS-generated velocity-gradient time series we examine the statistics of the infinitesimal material elements at steady state, employing an approach that is somewhat similar to that of Kraichnan (1974). Instead of dealing with the lengths, areas and volumes of infinitesimal elements we deal with length ratio $l(\equiv e(t)/e(0))$ and area ratio $A(\equiv f(t)/f(0))$. We also assess the performance of the stochastic velocity-gradient model of Girimaji & Pope (1990) in calculating the material-element deformation quantities. The following is a summary of our conclusions.

Mean growth rates

The estimate of the growth rate of the mean of $\ln l$ given by Batchelor (1952) is larger by a factor of three than the value calculated from DNS data, owing to the poor alignment of the line elements with the maximum positive strain-rate (a_1)

direction. The alignment of area elements with the maximum negative strain-rate (a_3) direction is also poor, resulting in the growth rate of $\ln A$ also being much smaller than expected. The poor alignment is caused by: (i) vorticity sweeping the material line away from the maximum positive strain-rate direction (figures 4 and 5); and (ii) the rotation of the principal-strain axes relative to the material lines (figure 6). The growth rates peak at about $2\tau_\eta$ before settling down to smaller steady-state values. This peaking is a result of the random initial distribution.

Kraichnan (1974) shows that if the velocity field is reflection-invariant the statistics of the growth rates of the logarithms of length ratio and area ratio would be identical. The steady-state growth rates of $\ln l$ and $\ln A$ are different by about 20%, showing that the turbulence velocity field (generated by DNS) is not quite reflection-invariant, as was indeed noted by Kraichnan (1974).

P.d.f. of l and A

The p.d.f.s of $l/\langle l\rangle$ and $A/\langle A\rangle$ do not attain stationarity (figures 8, 9 and 10) as hypothesized by Batchelor (1952). It is shown analytically that if the variance and the integral timescale of ζ (or ξ) are non-zero, then $l/\langle l\rangle$ (and similarly $A/\langle A\rangle$) cannot be statistically stationary. Figures 11–13 show that in homogeneous isotropic turbulence the variance and integral timescale of ζ and ξ are indeed non-zero. Then the relevant lengthscales that govern the evolution of line elements are $e(0)\exp(\langle\zeta\rangle t)$ and $e(0)\exp[(\mathrm{var}\,(\zeta)T_\zeta t)^{\frac{1}{2}}]$. The second lengthscale indicates the extent of departure of the random variable $l/\langle l\rangle$ from stationarity. If the first of these two lengthscales were much larger than the second, Batchelor's scaling would have led to a nearly stationary random variable. However, from DNS, $\langle\zeta\rangle \approx 0.13$ and $(T_\zeta \mathrm{var}\,\zeta)^{\frac{1}{2}} \approx 0.22$, indicating that the second length is at least as important as the first.

The central limit theorem suggests that the p.d.f.s of parameters $\hat{l}$ and $\hat{A}$ defined by (27) and (28) would assume stationary Gaussian distributions at steady state and calculations from DNS data (figures 14, 15, 16 and 17) indicate that such is indeed the case. (Kraichnan 1974 comes to the same conclusion for the case when the velocity field is a white-noise process.) The mean and variance of $\ln l$ and $\ln A$ grow linearly in time, at rates that are almost independent of Reynolds number (table 2). Moreover the steady-state p.d.f.s of $\hat{l}$ and $\hat{A}$ appear nearly independent of Reynolds number (figures 18 and 19) which in fact is inevitable if the central limit theorem governs the probability distribution of the integrals of ζ and ξ. If $\hat{l}$ and $\hat{A}$ are Gaussian, expressions for the various moments of l and A can be derived if the statistical properties of ζ and ξ are known. The pth moment of l at a time t is given by

$$\langle l^p\rangle(t) \approx \exp[p\langle\ln l\rangle(t) + (p^2/2)\,\mathrm{var}\,(\ln l(t))]. \tag{35}$$

If it can be further assumed that

$$\langle\ln l\rangle(t) \approx \langle\zeta\rangle t, \tag{36}$$

$$\mathrm{var}\,(\ln l(t)) \approx 2\,\mathrm{var}\,(\zeta)\,T_\zeta t, \tag{37}$$

the exponent Γ_p defined by Drummond & Münch (1990*a*) can be calculated:

$$\Gamma_p = \frac{1}{p\langle l^p\rangle}\frac{\mathrm{d}\langle l^p\rangle}{\mathrm{d}t} = \langle\zeta\rangle + p\,\mathrm{var}\,(\zeta)\,T_\zeta. \tag{38}$$

A similar derivation is also valid for the area-ratio moments.

Material-volume deformation

The angles θ and α (see §1.2 for definition) are of interest. Their statistics, however, are completely determined by the statistics of ζ and ξ. The sine of the angle between two initially mutually perpendicular material lines decreases approximately exponentially ($\sin\theta(t) \approx \exp(-0.1t)$). The cosine of the angle between the normal to a material plane and a material line that was initially normal to the material plane also decreases exponentially ($\cos\alpha(t) \approx \exp(-0.3t)$). The estimated steady-state growth rates of the eigenvalues of the Cauchy–Green tensor are given by (32)–(34). These estimates account for vorticity and non-persistent straining. As shown in figure 20 (see table 3 also) these estimates are quite accurate. The logarithm of the intermediate eigenvalue ($\ln(w_2)$) is in general positive and small in magnitude compared to $\ln(w_1)$ and $\ln(w_3)$.

Performance of diffusion model

The performance of the model in calculating the mean and variance of ζ and ξ is good (figure 21). The integral timescale of the two-time correlation of the model ζ is smaller than that of DNS by about 17% (figure 22), resulting in a slower growth of the model var($\ln l$). The integral timescale of the model ξ is larger than that of DNS by 17%. However, the steady-state model p.d.f.s of $\hat{l}$ and $\hat{A}$ agree quite well with the corresponding DNS p.d.f.s (figures 18 and 19). The eigenvalues of the Cauchy–Green tensors are also calculated fairly well by the model (figure 23).

Higher Reynolds numbers

The comparison of various Reynolds numbers (< 100) shows that to within statistical errors, ζ scales as τ_η^{-1} and the integral timescale T_ζ as τ_η. This scaling is likely to be valid for all Reynolds numbers, so that the ratio of the two relevant lengthscales in the problem – $e(0)\exp(\langle\zeta\rangle t)$ and $e(0)\exp[(\mathrm{var}(\zeta))^{\frac{1}{2}} T_\zeta t)^{\frac{1}{2}}]$ – is independent of the Reynolds number. The probability distribution of $\hat{l}$ is likely to continue to be amenable to the central limit theorem, resulting in l also being log-normally distributed at high Reynolds number. Similar arguments are also valid for the area ratio.

This work was supported by the US Air Force Office of Scientific Research (grant number AFOSR-88-0052). Computations conducted during the research were performed on the Cornell National Supercomputer Facility, which is supported in part by the National Science Foundation, New York State, the IBM Corporation and the members of the Corporate Research Institute.

Appendix. Numerical algorithm used to determine $\boldsymbol{B}$

In this Appendix the algorithm used to integrate (12) for the tensor $\boldsymbol{B}$ is discussed. The incompressibility condition requires that the determinant of $\boldsymbol{B}$ be unity. The numerical satisfaction of this condition requires that $\boldsymbol{B}$ be updated very accurately. This is achieved using the following fourth-order Runge–Kutta scheme:

$$B^1_{ij}(t) = B_{ij}(t) + \tfrac{1}{2}\Delta t\, h_{ik}(t) B_{kj}(t), \tag{A 1}$$

the backward Euler corrector step:

$$B^2_{ij}(t) = B_{ij}(t) + \tfrac{1}{4}\Delta t\,[h_{ik}(t) + h_{ik}(t+\Delta t)] B^1_{kj}(t), \tag{A 2}$$

the mid-point predictor step:

$$B^3_{ij}(t) = B_{ij}(t) + \tfrac{1}{2}\Delta t\,[h_{ik}(t) + h_{ik}(t+\Delta t)]\,B^2_{kj}(t), \tag{A 3}$$

and the Simpson corrector step

$$B_{ij}(t+\Delta t) = B_{ij}(t) + \tfrac{1}{6}\Delta t\,[h_{ik}(t)B_{kj}(t) + \{h_{ik}(t) + h_{ik}(t+\Delta t)\}\{B^1_{kj} + B^2_{kj}\} + h_{ik}(t+\Delta t)B^3_{kj}(t)]. \tag{A 4}$$

This scheme is found to give the required degree of accuracy.

REFERENCES

Ashurst, W. T., Kerstein, A. R., Kerr, R. M. & Gibson, C. H. 1987 Alignment of vorticity and scalar gradient in simulated Navier–Stokes turbulence. *Phys. Fluids* **30**, 2343.

Batchelor, G. K. 1952 The effect of homogeneous turbulence on material lines and surfaces. *Proc. R. Soc. Lond.* A **213**, 349.

Batchelor, G. K. & Townsend, A. A. 1956 Turbulent diffusion. In *Surveys in Mechanics* (ed. G. K. Batchelor & R. M. Davies), p. 352. Cambridge University Press.

Cocke, W. J. 1969 Turbulent hydrodynamic line stretching: consequences of isotropy. *Phys. Fluids* **12**, 2448.

Drummond, I. T. & Münch, W. 1990*a* Turbulent stretching of material elements. *J. Fluid Mech.* **215**, 45.

Drummond, I. T. & Münch, W. 1990*b* Distortion of line and surface elements in turbulent flows. *J. Fluid Mech.* (submitted).

Eswaran, V. & Pope, S. B. 1988 An examination of forcing in direct numerical simulations of turbulence. *Comput. Fluids* **16**, 257.

Girimaji, S. S. & Pope, S. B. 1990 A diffusion model for velocity gradients in homogeneous, isotropic turbulence. *Phys. Fluids* A **2**, 242.

Kraichnan, R. H. 1974 Convection of a passive scalar by a quasi-uniform random straining field. *J. Fluid Mech.* **64**, 737.

Lumley, J. L. 1972 On the solution of equations describing small scale deformation. *Symposia Mathemetica* (Istituto Nazionale di Alta Matematica), Vol. 9, pp. 315–334.

Monin, A. S. & Yaglom, A. M. 1981 *Statistical Fluid Mechanics*, Vol. 2 (ed. J. L. Lumley), Section 24.5, p. 578. MIT Press.

Orszag, S. A. 1970 Comments on Turbulent hydrodynamic line stretching: consequences of isotropy. *Phys. Fluids* **13**, 2203.

Pope, S. B. 1988 The evolution of surfaces in turbulence. *Intl J. Engng Sci.* **26**, 445–469.

Pope, S. B., Yeung, P. K. & Girimaji, S. S. 1989 The curvature of material surfaces in isotropic turbulence. *Phys Fluids* A **1**, 2010.

Rogallo, R. S. 1981 Numerical experiments in homogeneous turbulence. *NASA TM* 81315.

Tennekes, H. & Lumley, J. L. 1975 *A First Course in Turbulence.* MIT Press.

Townsend, A. A. 1951 The diffusion of heat sports in isotropic turbulence. *Proc. R. Soc. Lond.* A **209**, 418.

Yeung, P. K., Girimaji, S. S. & Pope, S. B. 1990 Straining and scalar dissipation on material surfaces in turbulence: implications for flamelets. *Combust. Flame* **79**, 340.

Yeung, P. K. & Pope, S. B. 1988 An algorithm for tracking fluid particles in numerical simulations of homogeneous turbulence. *J. Comput. Phys.* **79**. 373.

Yeung, P. K. & Pope, S. B. 1989 Lagrangian statistics from direct numerical simulations of isotropic turbulence. *J. Fluid Mech.* **207**, 531.